

# Radiation Pressure Confinement - I. Ionized Gas in the ISM of AGN Hosts

Jonathan Stern,\* Ari Laor and Alexei Baskin

*Department of Physics, Technion – Israel Institute of Technology, Haifa 32000, Israel*

11 March 2022

## ABSTRACT

We analyze the hydrostatic effect of AGN radiation pressure on optically thick gas in the host galaxy. We show that in luminous AGN, the radiation pressure likely confines the ionized layer of the illuminated gas. Radiation pressure confinement (RPC) has two main implications. First, the gas density near the ionization front is  $7 \times 10^4 L_{i,45} r_{50}^{-2} \text{cm}^{-3}$ , where  $L_{i,45}$  is the ionizing luminosity in units of  $10^{45} \text{erg s}^{-1}$  and  $r_{50}$  is the distance of the gas from the nucleus in units of 50 pc. Second, as shown by Dopita et al., the solution of the ionization structure within each slab is unique, independent of the ambient pressure. We show that the RPC density vs. distance relation is observed over a dynamical range of  $\sim 10^4$  in distance, from sub-pc to kpc from the nucleus, and a range of  $\sim 10^8$  in gas density, from  $10^3$  to  $10^{11} \text{cm}^{-3}$ . This relation implies that the radiative force of luminous AGN can compress giant molecular clouds in the host galaxy, and possibly affect the star formation rate. The unique ionization structure in RPC includes a highly ionized X-ray emitting surface, an intermediate layer which emits coronal lines, and a lower ionization inner layer which emits optical lines. This structure can explain the observed overlap of the extended X-ray and optical narrow line emission in nearby AGN. We further support RPC by comparing the predicted ratios of the narrow lines strength and narrow line widths with available observations. We suggest a new method, based on the narrow line widths, to estimate the black hole mass of low luminosity AGN.

**Key words:**

## 1 INTRODUCTION

Observations of emission lines in active galaxies point to the presence of photoionized gas in a wide range of radii, ionization states, gas densities and velocities. The radii  $r$ , H nuclei densities  $n$ , and velocities  $v$  seem to be strongly coupled, with dense  $n \sim 10^9\text{--}11 \text{cm}^{-3}$  and fast  $v \sim 3000 \text{km s}^{-1}$  ionized gas appearing on sub-pc scales (the broad line region, or BLR), while lower  $v \sim 300 \text{km s}^{-1}$  and lower  $n \sim 10^{2\text{--}5} \text{cm}^{-3}$  ionized gas appears at scales of tens of parsecs to several kiloparsecs (the narrow line region, or NLR). In some low luminosity active galactic nuclei (AGN), an intermediate region with  $v \sim 1000 \text{km s}^{-1}$  and  $n \sim 10^{6\text{--}8} \text{cm}^{-3}$  is also observed (Filippenko & Halpern 1984; Filippenko 1985; Appenzeller & Oestreicher 1988; Ho et al. 1996). This decrease of  $n$  and  $v$  with increasing  $r$  seems to appear also within specific regions. Resolved observations of the NLR show  $n$  increases towards the nucleus (Kraemer et al. 2000; Barth et al. 2001; Bennert et al. 2006a,b; Walsh et al. 2008; Stoklasová et al. 2009), while the unresolved intermediate line region shows an increase of  $n$  with  $v$  (see Filippenko & Halpern 1984 and citations thereafter). An association of  $v$  with  $r$  is expected if the gas kinematics near the center are

dominated by the black hole gravity, but what causes the association of  $n$  with  $r$ ?

On the other hand, the large scale stratification seen in  $n$  is not observed in the ionization state. Quite the contrary is true – in both the NLR and the BLR ions from a wide range of ionization potentials (IP) are commonly observed, including narrow lines of [S II] (IP=10 eV), [O III] (IP=35 eV), [Ne V] (97 eV), Fe X (234 eV), and broad lines of Mg II (8 eV), C IV (48 eV), O VI (114 eV) and Ne VIII (207 eV). Moreover, resolved maps of emission lines with widely different IP indicate that the high ionization gas and low ionization gas are co-spatial. A strong spatial correlation is seen between the high IP extended X-ray line emission and the relatively low IP [O III] emission (Young et al. 2001; Bianchi et al. 2006; Massaro et al. 2009; Dadina et al. 2010; Balmaverde et al. 2012). A similar correlation is also seen between the optical and near infrared high IP emission and the [O III] emission (Mazzalay et al. 2010, 2013). The co-spatiality of the high ionization and low ionization gas suggests a common origin of these two components.

Also, in mid infrared emission lines, where extinction effects are minimal, high IP and low IP lines exhibit a very small dispersion in their luminosity ratios. The [Ne V]  $14.32 \mu\text{m}$ , [O IV]  $25.89 \mu\text{m}$  and [Ne III]  $15.55 \mu\text{m}$  emission lines have IPs of 97 eV, 55 eV and 41 eV respectively, but the dispersion in their luminosity ratios between different objects is  $\lesssim 0.2$  dex

\* E-mail: stern@physics.technion.ac.il (JS); laor@physics.technion.ac.il (AL); alexei@physics.technion.ac.il (AB)

(Gorjian et al. 2007; Meléndez et al. 2008; Weaver et al. 2010). This small dispersion also suggests a common origin for the low ionization and high ionization gas. Why is low ionization gas always accompanied by high ionization gas, and vice-versa?

A possible physical source of the characteristics mentioned above is the mechanism which confines the ionized layer of the illuminated gas. On the back side, beyond the ionization front, cool dense gas can supply the confinement. However, an optically thin confining mechanism is required at the illuminated surface. Several optically thin confining mechanisms have been suggested for the ionized gas in AGN, usually for a specific region. A hot low  $n$  medium in pressure equilibrium with cooler line-emitting gas has been proposed for the BLR (Krolik et al. 1981; Mathews & Ferland 1987; Begelman et al. 1991), and for the NLR (Krolik & Vrtilik 1984). Other proposed confining mechanisms include a low density wind striking the face of the gas (e.g. Whittle & Saslaw 1986), and a magnetic field permeating the intercloud medium (Rees 1987 and Emmering et al. 1992 for the BLR; de Bruyn & Wilson 1978 for the NLR). Most of the above suggestions require an additional component for confining the gas, implying that the gas pressure is an independent free parameter.

However, one source of confinement is inevitable in a hydrostatic solution, and incurs no additional free parameters. Photoionization must be associated with momentum transfer from the radiation to the gas. Thus, the pressure of the incident radiation itself can confine the ionized layer of the illuminated gas, without requiring any additional components. In this simpler scenario, where the gas is radiation pressure confined (RPC), the gas pressure is set by the flux of the incident radiation.

Dopita et al. (2002, hereafter D02), Groves et al. (2004a), and Groves et al. (2004b, hereafter G04) showed that the gas pressure in the NLR gas is likely dominated by radiation pressure. They derived a slab structure where the ionization decreases with depth, which implies a common source for low IP and high IP emission lines. Also, this slab structure implies that the low ionization layer sees an absorbed spectrum, as observed in some nearby AGN (Kraemer et al. 2000, 2009; Collins et al. 2009). Building on the work of D02 and G04, we show that in RPC the same slab of gas which emits the low ionization emission lines can have a highly ionized surface which emits X-rays lines. We show that because the gas pressure is not an independent parameter, this slab structure is unique over a large range of  $r$  and other model parameters. This specific structure is likely responsible for the tight relation between the low IP emission lines and the high IP lines observed in the X-ray, optical and IR.

If the ionized gas is RPC, then the pressure at the ionization front, where most of the ionizing radiation is absorbed, equals the incident radiation pressure, which is  $\propto r^{-2}$ . Since the temperature near the ionization front is  $\sim 10^4$  K, RPC implies  $n \propto r^{-2}$ . We show below that this  $n \propto r^{-2}$  relation quantitatively reproduces the decrease of  $n$  with  $r$  seen in resolved observations of the NLR, and the increase of  $n$  with  $\nu$  seen in the unresolved intermediate line region. In a companion paper (Baskin et al. 2013, hereafter Paper II) we show that RPC also reproduces  $n$  at the BLR. Together, these findings imply that RPC sets  $n$  of ionized gas in active galaxies over a dynamical range of  $\sim 10^4$  in  $r$ , from sub-pc to kpc scale, and a dynamical range of  $\sim 10^8$  in  $n$ , from  $10^3$  to  $10^{11}$  cm $^{-3}$ .

Hydrostatic radiation pressure effects were also applied to models of ionized gas in star forming regions (Pellegrini et al. 2007, 2011; Draine 2011a; Yeh et al. 2013; Verdolini et al. 2013), and to models of ‘warm absorbers’, i.e. ionized gas in AGN de-

tected in absorption (Rózańska et al. 2006; Chevallier et al. 2007; Gonçalves et al. 2007).

The paper is built as follows. In §2.1 we present the necessary conditions for RPC. In §2.2 – §2.6, we derive several analytical results from these conditions. We use CLOUDY (Ferland et al. 1998) to carry out detailed numerical calculations. The emission line emissivities vs.  $r$  implied by RPC are presented in §2.7. In §3 we compare the RPC calculations with available observations. In §4, we analyze the observational and theoretical evidence for the existence of dust in the ionized gas, which has a strong effect on the structure of RPC slabs. We discuss our results and their implications in §5, and conclude in §6.

## 2 RADIATION PRESSURE CONFINEMENT

### 2.1 Conditions for RPC

We assume a one dimensional, hydrostatic, semi-infinite slab of gas. The slab is assumed to be moving freely in the local gravitational field, so external gravity is canceled in the slab frame of reference. The ionized layer of this slab is confined by radiation pressure if it satisfies two conditions. The first condition is that the force applied by the radiation needs to be the strongest force applied to the gas. Under this condition, the hydrostatic equation is

$$\frac{dP_{\text{gas}}}{dx} = \beta \frac{F_{\text{rad}}}{c} n \bar{\sigma} \quad (1)$$

where  $P_{\text{gas}}$  is the gas pressure,  $x$  is the depth into the slab measured from the illuminated surface,  $F_{\text{rad}}$  is the flux of ionizing radiation at  $x$ , and  $\bar{\sigma}$  is the sum of the mean absorption and scattering opacity per H nucleus, weighted by the ionizing flux. We define a correction factor  $\beta$ , which accounts for the additional radiative force due to the absorption of non-ionizing photons in the ionized layer, and the correction due to anisotropic scattering. We show below that for a typical AGN spectral energy distribution (SED),  $\beta \sim 1$  in dust-less gas and  $\beta \sim 2$  in dusty gas. Other sources of pressure, including magnetic pressure and the pressure of the trapped emitted radiation, are assumed to be small compared to  $P_{\text{gas}}$ .

The second condition, presented by D02, is that the radiation pressure needs to be significantly larger than the ambient pressure, i.e.,

$$\beta P_{\text{rad}} \gg P_{\text{gas},0} \quad (2)$$

where  $P_{\text{rad}}$  is the pressure of the ionizing radiation at the illuminated surface ( $P_{\text{rad}} = L_{\text{ion}}/4\pi r^2 c$ ,  $L_{\text{ion}}$  is the luminosity at 1 – 1000 Ryd). For properties which are defined as a function of  $x$ , such as  $P_{\text{gas}}$ , we use a subscript ‘0’ to denote a value of a certain variable at the illuminated surface, and a subscript ‘f’ to denote a value near the ‘ionization front’ – the boundary between the H II and H I layers.

At the ionization front, most of the ionizing radiation has been absorbed, therefore equations 1 and 2 imply that

$$P_{\text{gas},f} = P_{\text{gas},0} + \beta P_{\text{rad}} \approx \beta P_{\text{rad}} \quad (3)$$

where we assumed that  $x_f \ll r$ , so  $P_{\text{rad}}$  is not geometrically diluted with increasing  $x$  (see §2.6).

The natural units to discuss RPC is  $\Xi \equiv \beta P_{\text{rad}}/P_{\text{gas}}$ . This definition of  $\Xi$  differs from the common definition (Krolik et al. 1981) by a factor of  $\beta$ , which is the natural extension for including the effect of pressure from non-ionizing radiation. Also, we follow D02 and drop the factor of 2.3 in the original definition. In these units,

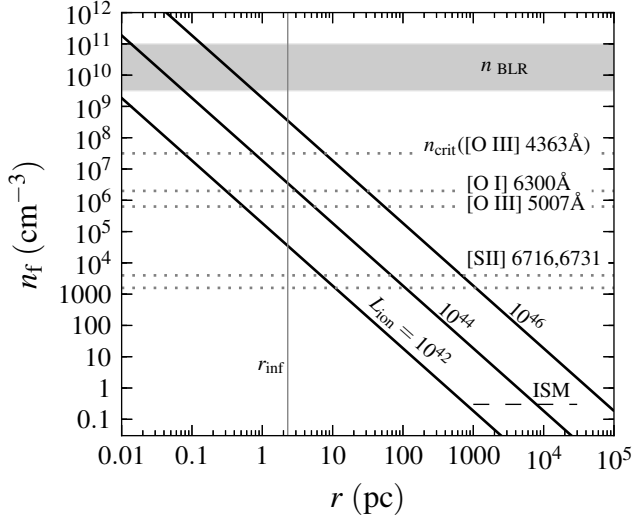


**Figure 1.** The gas density near the ionization front implied by RPC, versus the distance from the AGN and the AGN luminosity. Thick solid lines show the  $n_f \propto r^{-2}$  relation (eq. 6) for different  $L_{\text{ion}}$  (noted in  $\text{erg s}^{-1}$ ). For comparison, we plot the typical  $n$  of the BLR (gray stripe), the  $n_{\text{crit}}$  of various forbidden lines (dotted lines), the gravitational radius of influence for  $M_{\text{BH}} = 10^8 M_{\odot}$  (solid gray, see §3.2), and the typical ISM pressure in the solar neighborhood, in units of  $T_4 \text{ cm}^{-3}$  (short dashed line). The AGN radiation pressure is larger than the typical ISM pressure at  $r < 25 L_{i,45}^{1/2} \text{ kpc}$ . Since forbidden line emission drops at  $n > n_{\text{crit}}$ , RPC implies a stratification of line emission according to  $n_{\text{crit}}$ . In low luminosity AGN, high  $n_{\text{crit}}$  lines will be emitted from  $r < r_{\text{inf}}$ , and will have a wider profile than expected from  $\sigma_*$ .

equations 2 and 3 are simply

$$\Xi_0 \gg 1 \quad (4)$$

and

$$\Xi_f = 1 \quad (5)$$

## 2.2 The $n$ near the ionization front

Near the ionization front,  $T_f \approx 10^4 \text{ K}$  to within a factor of  $\lesssim 2$  (e.g. Krolik 1999). Therefore, using  $P_{\text{gas},f} = 2.3n_f K_B T_f$  and  $\beta = 2$ , eq. 3 implies

$$n_f = 7.4 \times 10^4 \frac{L_{i,45}}{r_{50}^2} T_{f,4}^{-1} \text{ cm}^{-3} \quad (6)$$

where  $L_{\text{ion}} = 10^{45} L_{i,45} \text{ erg s}^{-1}$ ,  $r = 50 r_{50} \text{ pc}$  and  $T_f = 10^4 T_{f,4} \text{ K}$ . Note that  $n_f$  is independent of  $n_0$ .

Equation 6 is plotted in Figure 1 for different  $L_{\text{ion}}$ , assuming  $T_{f,4} = 1$ . For comparison, we plot the typical ISM pressure in the solar neighborhood,  $nT_4 = 0.3 \text{ cm}^{-3}$  (Draine 2011b). The pressure induced by the AGN radiation is stronger than the ISM pressure at  $r < 25 L_{i,45}^{1/2} \text{ kpc}$ . Therefore, the radiation pressure of Seyferts will likely have a significant effect on the ISM of the whole host galaxy, while Quasars can also significantly affect the pressure equilibrium in the circum-galactic medium.

Fig. 1 also shows the critical densities  $n_{\text{crit}}$  of various forbidden lines with relatively low ionization levels. For a broad distribution of  $n$ , the emission of a certain forbidden line is expected to peak at gas with  $n \sim n_{\text{crit}}$  (but see a refinement in §2.7). The low

ionization levels of these lines ensure they are emitted near the ionization front, so  $n_f$  is a measure of  $n$  where these lines are emitted. Therefore, eq. 6 implies that the forbidden line emission peaks at  $r \sim 14 (L_{i,45}/n_{\text{crit},6})^{1/2} \text{ pc}$ , where  $n_{\text{crit}} = 10^6 n_{\text{crit},6}$ . For a specific  $L_{\text{ion}}$  and forbidden line, the radius of peak emission can be read from the intersection of the appropriate solid and dotted lines in Fig. 1. Hence, RPC implies that the emission of forbidden lines should be stratified in  $r$  according to their  $n_{\text{crit}}$ . For example, the high  $n_{\text{crit}}$  [O III]  $\lambda 4363$  line will be emitted from gas with  $r$  which is 100 times smaller than the the gas which emits the low  $n_{\text{crit}}$  [S II] doublet. In §3, we compare eq. 6 with narrow line observations.

Also shown in Fig. 1 is the range of  $n$  observed in the BLR,  $n_{\text{BLR}} = 10^{9.5-11} \text{ cm}^{-3}$  (Davidson & Netzer 1979; Rees et al. 1989; Ferland et al. 1992; Marziani et al. 1996). The BLR is within the dust sublimation radius (Netzer & Laor 1993; Suganuma et al. 2006), so  $\beta(\text{BLR}) \sim 1$ , lower by a factor of two than assumed in Fig. 1.

## 2.3 The effective $U$ near the ionization front

D02 showed that eq. 3 implies an effective  $U_f \sim 0.01$ . For completeness, we repeat their derivation here with our notation. We denote the average energy per ionizing photon as  $\langle h\nu \rangle$ , and the volume density of incident ionizing photons as  $n_\gamma (= L_{\text{ion}}/4\pi r^2 c \langle h\nu \rangle)$ . From eq. 3 we get

$$\begin{aligned} 2.3n_f K_B T_f &= \beta \frac{L_{\text{ion}}}{4\pi r^2 c} = \beta n_\gamma \langle h\nu \rangle \Rightarrow \\ U_f \equiv \frac{n_\gamma}{n_f} &= \frac{2.3K_B T_f}{\beta \langle h\nu \rangle} = 0.03 T_{f,4} \frac{72 \text{ eV}}{\beta \langle h\nu \rangle} \end{aligned} \quad (7)$$

The numerical value of  $\langle h\nu \rangle = 36 \text{ eV}$  is appropriate for an ionizing slope of  $-1.6$ , as seen in luminous AGN (Telfer et al. 2002). We emphasize that  $n_\gamma$  is measured at the illuminated surface, before any absorption has occurred. Using  $n_\gamma/n_f$  for the effective  $U_f$  is reasonable, since most of the absorption occurs near the ionization front, where  $\tau \sim 1$  and  $n \sim n_f$  (see D02 and next section). Therefore, eq. 7 implies that at  $x \sim x_f$  RPC gas is similar to constant  $n$  gas with an initial ionization parameter  $U_0 \equiv n_\gamma/n_0 \sim 0.03$ . This effective  $U$  is independent of the boundary conditions  $n_0$  and  $n_\gamma$ , and therefore a general property of RPC gas. The value of  $U_f$  is set only by the ratio of the gas pressure per H-nucleus ( $2.3K_B T$ ) to the pressure per ionizing photon ( $\beta \langle h\nu \rangle$ ).

Using eq. 7, D02 showed that in Seyferts the derived values of  $U$  and the small dispersion in  $U$  between different objects suggests that the NLR gas is RPC. In Paper II, we use a similar argument to show that the BLR gas is also RPC.

## 2.4 The slab structure vs. $\tau$

### 2.4.1 Analytical derivation

In the optically thin layer at the illuminated surface of the slab,  $F_{\text{rad}}$  is constant as a function of  $x$  and equals to  $F_{\text{rad},0}$ . Hence,  $F_{\text{rad}}/c = P_{\text{rad}}$ , and the hydrostatic equilibrium equation (eq. 1) can be expressed as

$$\frac{dP_{\text{gas}}}{dx} = \beta P_{\text{rad}} n \bar{\sigma} \quad (8)$$

Assuming that  $\beta$  does not change significantly with  $x$ , equation 8 can be solved by switching variables to the optical depth  $d\tau = n\bar{\sigma} dx$ :

$$\frac{dP_{\text{gas}}}{d\tau} = \beta P_{\text{rad}} \Rightarrow P_{\text{gas}}(\tau) = P_{\text{gas},0} + \beta P_{\text{rad}} \tau \quad (9)$$

For  $P_{\text{gas},0}/\beta P_{\text{rad}} \ll \tau \ll 1$  we get

$$P_{\text{gas}}(\tau) = \beta P_{\text{rad}} \tau \quad (10)$$

or equivalently, for  $\Xi_0^{-1} \ll \tau \ll 1$  we get

$$\Xi(\tau) = \frac{1}{\tau} \quad (11)$$

Equation 11 implies that in RPC,  $\Xi$  has a specific value at each  $\tau$ , independent of other model parameters. Since the ionization state of the gas is determined to first order by  $\Xi$ , eq. 11 implies a very specific ionization structure for RPC gas, in which the surface layer is highly ionized (high  $\Xi$ ) and ionization decreases with increasing  $\tau$ .

For comparison with observations, one needs to know the fraction of the power  $W$  emitted in each ionization state. The emission from each layer is equal to the energy absorbed in the layer. However, in a semi-infinite slab only roughly half the power emitted from a certain layer escapes the slab without further absorption. Therefore,

$$\frac{dW(\Xi)}{d \log \Xi} = 0.5 \frac{d\tau}{d \log \Xi} = 0.5 \Xi^{-1} \quad (12)$$

where the last equality is derived from eq. 11. Eq. 12 gives directly the fraction of the power emitted in each ionization state, e.g. about 0.5% of the emission comes from  $\log \Xi \sim 2$  gas, and  $\sim 5\%$  of the emission comes from  $\log \Xi \sim 1$  gas.

#### 2.4.2 CLOUDY calculations

To perform full CLOUDY calculations, we assume an incident spectrum and gas composition which we consider typical of the AGN and its environment, as follows. We use the Laor & Draine (1993) SED at  $\lambda > 1100\text{\AA}$ . We assume a power law with index  $-1$  at  $2-200\text{keV}$  (Tueller et al. 2008; Molina et al. 2009), and a cutoff at larger frequencies. The slope between  $1100\text{\AA}$  and  $2\text{keV}$  is parameterized by  $\alpha_{\text{ion}}$ . We run models both with and without dust grains, using the depleted ‘ISM’ abundance set and the default ‘solar’ abundance set, respectively. The actual abundances are scaled linearly with the metallicity parameter  $Z$  in all elements except Helium and Nitrogen. For the scaling of the latter two elements with  $Z$  we follow G04. We use the dust composition noted as ‘ISM’ in CLOUDY, and scale the dust to gas ratio with  $Z$ . We note that CLOUDY assumes that the radiation pressure on the dust is directly transferred to the gas. All CLOUDY calculations stop at a gas temperature  $T \sim 4000\text{K}$ , beyond which the H II fraction is  $< 0.1$  and there is only a negligible contribution to the emitted spectrum. We use the ‘constant total pressure’ flag, which tells CLOUDY to increase  $P_{\text{gas}}$  between consecutive zones<sup>1</sup>, according to the attenuation of the incident continuum (eq. 1).

In the dusty models, the calculated pressure due to the trapped line emission is always  $< 0.03 P_{\text{gas}}$ , justifying our assumption in §2.1 that it is negligible. However, in the dust-less models the line pressure can be comparable to  $P_{\text{gas}}$ , which causes stability problems in the CLOUDY calculation. We therefore turn off the line pressure in the dust-less calculations. In Paper II, we show that including line pressure in the dust-less models changes some of our derived quantities by a factor of  $\sim 2$ .

In order to compare the CLOUDY calculations with our analytical derivations above, we need to calculate  $x_f$ ,  $\tau$ , and  $\beta$ . We set  $x_f$

<sup>1</sup> CLOUDY divides the slab into ‘zones’, and solves the local thermal equilibrium and local ionization equilibrium equations in each zone.

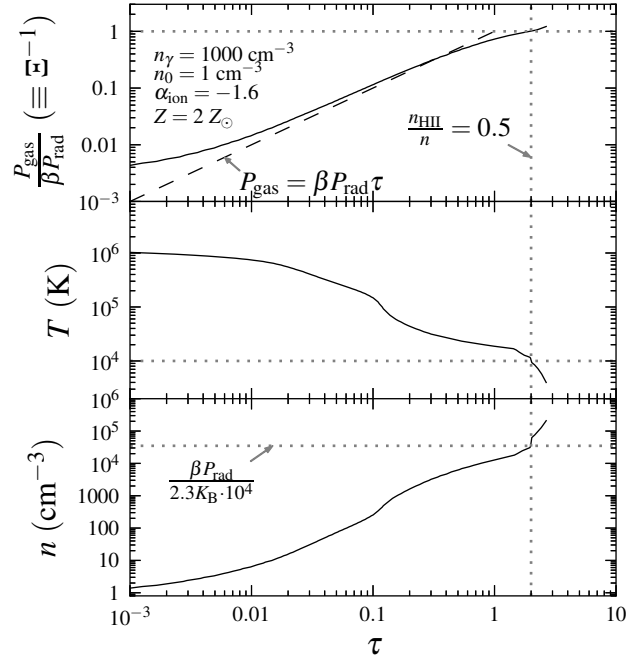


**Figure 2.** The slab structure of an RPC slab, vs. optical depth. The solid line in each panel shows the result of the CLOUDY calculation, for the model parameters noted in the top panel. The vertical dotted line marks  $\tau_f$ , where the H ionized fraction is 50%. **(Top)** The  $P_{\text{gas}}$  structure. With the absorption of ionizing radiation,  $P_{\text{gas}}$  increases from  $P_{\text{gas},0}$  to  $P_{\text{gas},f} = \beta P_{\text{rad}}$  (eq. 3, horizontal dotted line). In this dusty model  $\beta = 1.9$  due to the absorption of optical photons by dust grains. The dashed line marks eq. 10, which is the analytical derivation of the slab structure assuming  $P_{\text{gas},0} \rightarrow 0$  and  $\tau \ll 1$ . Eq. 10 is similar to the CLOUDY calculation at  $0.01 \lesssim \tau \lesssim 1$ . **(Middle)** The  $T$  structure, which drops from  $10^6\text{K}$  at  $\tau = 0$  to  $10^4\text{K}$  (horizontal dotted line) at  $\tau = \tau_f$ . Over 80% of the absorption occurs at  $T < 40000\text{K}$ . **(Bottom)** The structure of  $n$ , which increases by four orders of magnitude at  $0 < \tau < 1$ , due to the increase in  $P_{\text{gas}}$  and the drop in  $T$ . The large range in  $n$  implies a large range in  $U$  within a single slab. The horizontal dotted line marks the expected  $n_f$  (eq. 6).

to be the  $x$  where the H ionized fraction is 50%. The value of  $\tau(x)$  is calculated by summing  $\Delta\tau(x')$  on all zones with  $x' < x$ , where  $\Delta\tau(x') = n(x')\bar{\sigma}(x')\Delta x'$ , and  $\Delta x$  is the width of the zone. In dusty models, the dust dominates the opacity, therefore  $\bar{\sigma}$  is constant to a factor of  $\sim 2$  at  $0 < x < x_f$ . In contrast, in dust-less models  $\bar{\sigma}$  is dominated by line absorption and bound-free edges, and therefore is a strong function of the ionization state, which changes significantly with increasing  $x$  (see below). The value of  $\beta$  is derived by comparing the total pressure induced by the radiation at  $x_f$  to the incident ionizing pressure  $P_{\text{rad}}$ .

Figure 2 shows the slab structure of a dusty model, with  $\alpha_{\text{ion}} = -1.6$ , typical of luminous AGN (Telfer et al. 2002), and  $Z = 2Z_{\odot}$ , the  $Z$  observed in the ISM of quiescent galaxies with stellar masses  $\sim 10^{11} M_{\odot}$ , which is likely the  $Z$  also found in the NLR of a typical AGN host (Groves et al. 2006; Stern & Laor 2013). We use  $n_{\gamma} = 1000\text{cm}^{-3}$ , which corresponds to  $r = 70 L_{1,45}^{1/2}\text{pc}$ . Different values of  $\alpha_{\text{ion}}$ ,  $Z$  or  $n_{\gamma}$  do not affect the conclusions of this section. We assume  $n_0 = 1\text{cm}^{-3}$ , so  $U_0 = 1000$  and  $\beta P_{\text{rad}}/P_{\text{gas}} = \Xi = 300$ , well within the RPC regime (eq. 2). The  $\beta$  in this model is equal to 1.9.

The top panel shows that  $P_{\text{gas}}$  increases from the assumed  $P_{\text{gas},0}$  at  $\tau = 0$  to  $\beta P_{\text{rad}}$  at  $\tau = \tau_f$  (eq. 3). Equation 10 (dashed line),



which is the analytical derivation of the slab structure assuming  $P_{\text{gas},0} \rightarrow 0$  and  $\tau \ll 1$ , is a good approximation of the CLOUDY calculation at  $0.01 \lesssim \tau \lesssim 1$ . Equivalently,  $\Xi$  decreases from 300 at  $\tau = 0$  to 1 at  $\tau = \tau_f$ , as expected from eqs. 11 and 5. Therefore, the analytical derivations of the slab structure vs.  $\tau$  agree with the full CLOUDY calculations.

The middle panel of Fig. 2 shows the  $T(\tau)$  profile, which drops from  $10^6$  K at  $\tau = 0$ , to  $10^4$  K (dotted line) at the ionization front. Note that  $T = 40000$  K at  $\tau = 0.2$ , therefore 80% of the absorption occurs in gas with  $T < 40000$  K. The bottom panel shows that  $n$  increases by four orders of magnitude at  $0 < \tau < 1$ , reaching the expected  $n_f$  (eq. 6) at the ionization front. This large increase in  $n$  is due to the increase in  $P_{\text{gas}}$  and the drop in  $T$ . The large change in  $n$  results in a large drop in  $U$ , from  $U_0 = 1000$  to  $U_f \approx 0.03$  (eq. 7). This large range in  $U$  is apparent in the Oxygen and Neon ionization structure within the slab, presented in Appendix A.

We note that the exact  $T(\tau)$  and  $n(\tau)$  profiles depend on the details of the dust physics and its interaction with the gas, which are subject to some uncertainty. Specifically, the solution at  $T \sim 10^5$  K may not be unique, and there could be two phases at the same pressure. We ignore this possibility here. However, the increase of  $P_{\text{gas}}$  with  $\tau$ , which is the main conclusion of this section, is independent of the exact  $T(\tau)$  profile.

Eq. 10 suggests that  $P_{\text{gas}}(\tau)$  is independent of the source of opacity, and therefore the  $P_{\text{gas}}(\tau)$  profile of dusty and dust-less models should be similar. Indeed, we find that the  $P_{\text{gas}}(\tau)$  of dust-less models are similar to the  $P_{\text{gas}}(\tau)$  of dusty models seen in the top panel of Fig. 2. We address the effect of dust in a more detailed manner in the following section, where we analyze the slab structure as a function of  $x$ , where the effect of dust is more prominent.

## 2.5 The slab structure vs. $x$

### 2.5.1 The pressure scale length

Eq. 8, which assumes  $\tau \ll 1$ , can be rewritten as

$$\frac{dP_{\text{gas}}}{dx} = \beta P_{\text{rad}} \bar{\sigma} \frac{P_{\text{gas}}}{2.3K_{\text{B}}T} \quad (13)$$

In order to tract the problem analytically, we assume that  $\bar{\sigma}$  and  $T$  do not change with  $x$ . The accuracy of this approximation will become apparent below, where we compare the analytical result to the full CLOUDY calculation. Hence, eq. 13 can be integrated to

$$P_{\text{gas}}(x) = P_{\text{gas},0} e^{x/l_p} \quad (14)$$

or equivalently,

$$\Xi(x) = \Xi_0 e^{-x/l_p} \quad (15)$$

The pressure scale length,  $l_p$ , is equal to

$$l_p = \frac{2.3K_{\text{B}}T}{\beta P_{\text{rad}} \bar{\sigma}} = 0.9 \bar{\sigma}_{-21}^{-1} T_6 \frac{r_{50}^2}{\beta L_{i,45}} \text{pc} \quad (16)$$

where  $T = 10^6 T_6$  K, the appropriate  $T$  at the illuminated surface (Fig. 2), and  $\bar{\sigma} = 10^{-21} \bar{\sigma}_{-21} \text{cm}^2$ . We show below that this value of  $\bar{\sigma}$  is typical of dusty gas, but is significantly lower in dust-less gas. Equivalently,  $l_p$  can be expressed with  $n_\gamma$  and  $\langle hv \rangle$ :

$$l_p = \frac{2.3K_{\text{B}}T}{\beta \langle hv \rangle n_\gamma \bar{\sigma}} = 1.8 \bar{\sigma}_{-21}^{-1} T_6 \frac{72 \text{eV}}{\beta \langle hv \rangle} n_{\gamma,3}^{-1} \text{pc} \quad (17)$$

where  $n_\gamma = 1000 n_{\gamma,3} \text{cm}^{-3}$ .

Within the slab,  $U$  is lower than at the illuminated surface. The decrease in  $U$  implies that  $T$  can only be lower within the slab than

at the surface, and we show below that  $\bar{\sigma}$  can only be higher within the slab than at the surface. Therefore, eqs. 16–17 imply that the largest  $l_p$  in the slab is at the illuminated surface.

The CLOUDY calculations of the slab structure at  $0 < x < x_f$  are shown in the left panels of Figures 3 and 4. As in Fig. 2, we use  $\alpha_{\text{ion}} = -1.6$ ,  $Z = 2Z_\odot$ , and  $n_{\gamma,3} = 1$ . The conclusions of this section are robust to other reasonable choices of  $\alpha_{\text{ion}}$  and  $Z$ , while the effect of changing  $n_\gamma$  is addressed in the following section. We analyze models with different  $n_0$  (or equivalently different  $U_0$  or different  $P_{\text{gas},0}$ ).

Fig. 3 shows the calculation of the dusty models. In the left panels, all models with  $U_0 \gg 0.03$  show a similar behavior. From a certain scale which is different in each model,  $P_{\text{gas}}$  and  $n$  significantly increase, reaching the same  $P_{\text{gas},f} = \beta P_{\text{rad}}$  (eq. 3) and  $n_f \approx \beta P_{\text{rad}} / 2K_{\text{B}} \cdot 10^4$  (eq. 6) at  $x = x_f$ . Therefore, the conditions at  $x = x_f$  are independent of the conditions at  $x = 0$ .

For comparison, we also calculate the analytical expression for  $P_{\text{gas}}(x)$  (eq. 14), which requires an evaluation of  $l_p$  at the illuminated surface. The value of  $l_p$  depends on  $\bar{\sigma}$ , which is dominated by the dust opacity at  $U_0 \gg 0.006$  (Netzer & Laor 1993), and equals to

$$\bar{\sigma}_{\text{dust}} = 0.8 \times 10^{-21} \frac{Z}{Z_\odot} \text{cm}^{-2} \quad (18)$$

for the assumed  $\alpha_{\text{ion}} = -1.6$ . We emphasize that this  $\bar{\sigma}$  is independent of  $U_0$  for  $U_0 \gg 0.006$ . Hence, for the models in Fig. 3, using eq. 17 we get  $l_p = 1.8 \times 10^{18} T_6 \text{cm}$ . The dashed lines in the top-left panel of Fig. 3 plot the analytical  $P_{\text{gas}}(x)$ . The analytical and CLOUDY calculations of  $P_{\text{gas}}(x)$  agree rather well. With increasing  $U_0$ ,  $l_p$  increases due to the increase in  $T_0$ . At  $x > l_p$ , the analytical expression somewhat underestimates  $P_{\text{gas}}(x)$ , due to the decrease in  $T$ , which is not accounted for in the analytical derivation.

In the  $U_0 = 0.01$  model  $P_{\text{gas},0} > P_{\text{rad}}$ , therefore  $P_{\text{gas},f} \approx P_{\text{gas},0}$ . This model is not RPC, since an additional source of confinement which is stronger than the radiation pressure is required to achieve  $P_{\text{gas}} > P_{\text{rad}}$ . The small dynamical range of  $n$  in this model implies that it is effectively a constant- $n$  model.

Fig. 4 shows the results of the CLOUDY calculation of the dust-less models. The models with  $U_0 \leq 10$  behave in a similar fashion as the dusty models. At  $x \approx l_p$ ,  $P_{\text{gas}}(x)$  significantly increases, reaching  $P_{\text{gas},f} = \beta P_{\text{rad}}$  at  $x = x_f$ . Here,  $\beta = 1.2$ . The  $l_p$  in the dust-less models are larger than in the dusty models, mainly due to the lower  $\bar{\sigma}$ <sup>2</sup>. We find that at  $U > 100$

$$\bar{\sigma}_{\text{es}} = \frac{n_e}{n} \sigma_{\text{Th}} = 0.9 \times 10^{-24} \text{cm}^2 \quad (19)$$

where  $\sigma_{\text{Th}}$  is the Thompson cross section. For lower  $U$ , line and edge opacity surpasses the electron scattering opacity, and  $\bar{\sigma}$  increases. In the  $U_0 = 1000$  model, the total column density at  $0 < x < x_f$  is  $3.6 \times 10^{22} \text{cm}^{-2}$ , implying that  $\bar{\sigma}$  averaged over the ionized layer is  $10^{-22.5} \text{cm}^2$ , a factor of 60 lower than the value of  $\bar{\sigma}$  in dusty gas (eq. 18).

In models with  $U_0 \geq 100$ ,  $l_p > 70 \text{pc}$ , which is larger than  $r$  for the assumed  $n_\gamma$  in an AGN with  $L_{i,45} = 1$ . Therefore, our assumption that  $x \ll r$  is violated. We address this constraint in §2.6.

<sup>2</sup> Also,  $T_0$  is lower in dusty models due to the cooling provided by dust-gas interactions. The effect of the different  $T$  on  $l_p$  is small compared to the effect of the different  $\bar{\sigma}$ .

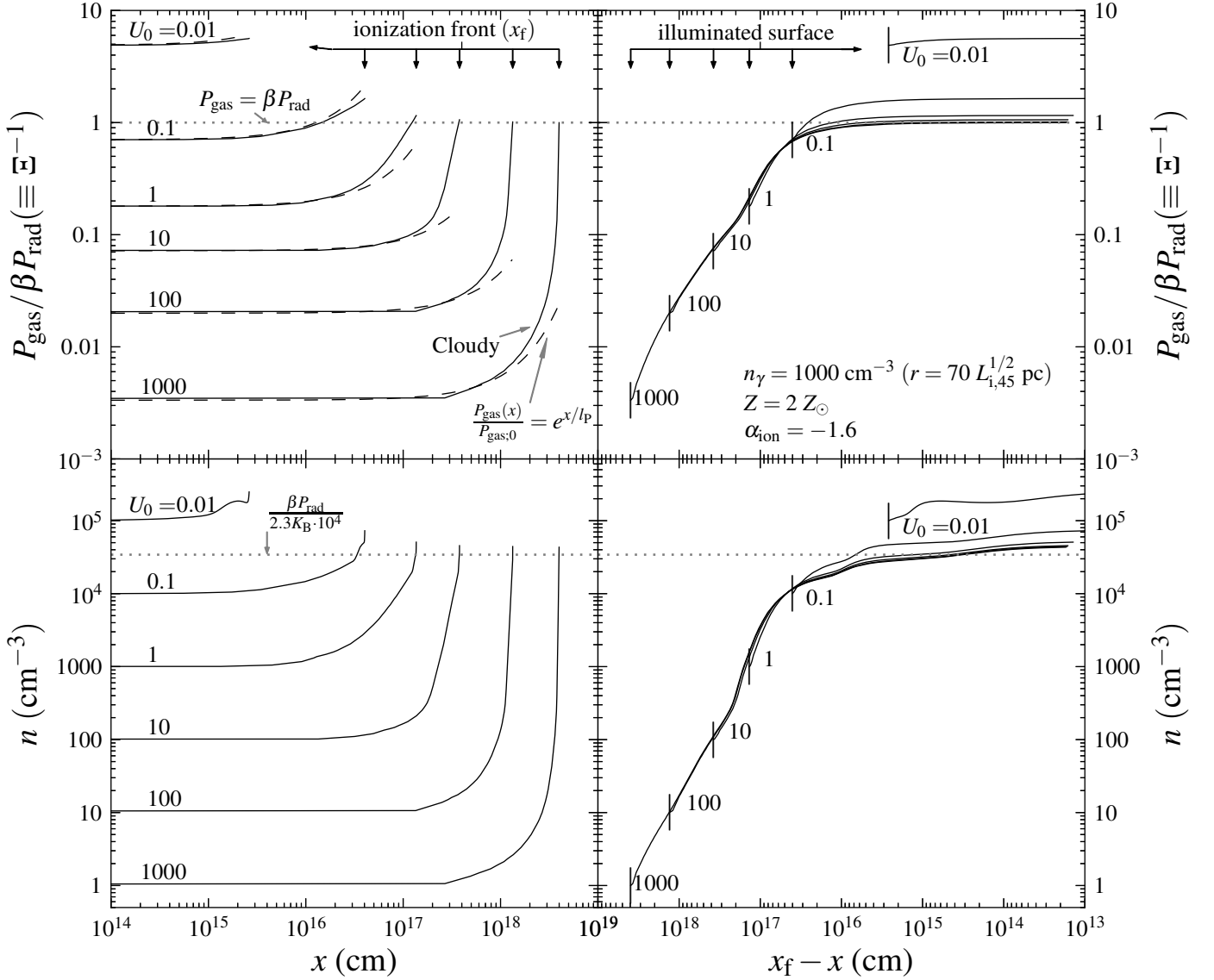


**Figure 3.** The structure of a dusty RPC slab vs. distance from the illuminated surface (left) and vs. distance from the ionization front (right). The solid lines show the results of the CLOUDY calculations at  $0 < x < x_f$ , for models with different  $U_0$  (noted near each line). Other model parameters are noted in the top-right panel. **(Left panels)** The value of  $P_{\text{gas}}$  and  $n$  increase with  $x$  as radiation is absorbed by the gas. Models with  $U_0 \gg 0.03$  (or  $\Xi_0 \gg 1$ ) have  $P_{\text{rad}} \gg P_{\text{gas},0}$ , and are therefore RPC. The  $P_{\text{gas},f}$  in all RPC models is independent of  $U_0$ , and equal to  $\beta P_{\text{rad}}$  (dotted line in the top panels). Similarly, in all RPC models  $n_f$  is independent of  $U_0$  and given by eq. 6 (dotted line in the bottom panels). In the  $U_0 = 0.01$  model  $P_{\text{gas},0} > P_{\text{rad}}$ , therefore this model is not RPC and requires an additional source of confinement. Dashed lines in the top-left panel plot eq. 14, the analytical expression for  $P_{\text{gas}}(x)$ . The increase in  $P_{\text{gas}}$  becomes significant at  $x \sim l_p$  (eq. 16), where  $l_p$  depends on  $U_0$ . The analytical and CLOUDY calculations give similar results. **(Right panels)** The illuminated surface of each model is noted by a ‘|’. All RPC models lie on the same  $P_{\text{gas}}(x_f - x)$  and  $n(x_f - x)$  profiles. That is, two RPC models with different boundary conditions  $n_0 = n'$  and  $n_0 = n'' > n'$  have the same solution at  $n > n''$ , and differ only in the existence of an optically thin surface layer with  $n' < n < n''$ . Therefore, RPC solutions are essentially independent of the boundary value  $n_0$  or  $U_0$ .

### 2.5.2 The slab structure vs. $x_f - x$

Above we showed that the  $P_{\text{gas}}(x)$  profiles of RPC models with different  $n_0$  differ, since  $l_p$  increases with  $U_0 \propto n_0^{-1}$ . However, Fig. 2 shows that  $n$  increases significantly already at  $\tau \ll 1$ . Therefore, if we compare two RPC models with different boundary conditions  $n_0 = n'$  and  $n_0 = n'' > n'$ , the former model should have an optically thin surface layer in which  $n' < n < n''$ . Since this surface layer is optically thin, we do not expect its existence to significantly affect

the solution at  $n > n''$ . In the inner layer where  $n > n''$ , the two RPC models should have similar solutions.

A similar solution at  $n > n''$  implies that if we present the slab structure as a function of distance from some depth *within* the slab, such as  $x_f - x$ , then solutions of models with different  $n_0$  should be practically identical, differing only in their starting point. In the right panels of Fig. 3 we show the slab structure of the dusty models vs.  $x_f - x$ . The illuminated surface of each model is noted by a ‘|’. All RPC models ( $U_0 \gg 0.03$ ) lie on the same  $P_{\text{gas}}(x_f - x)$  and  $n(x_f - x)$  profiles, differing only in the  $x_f - x$  value of the il-

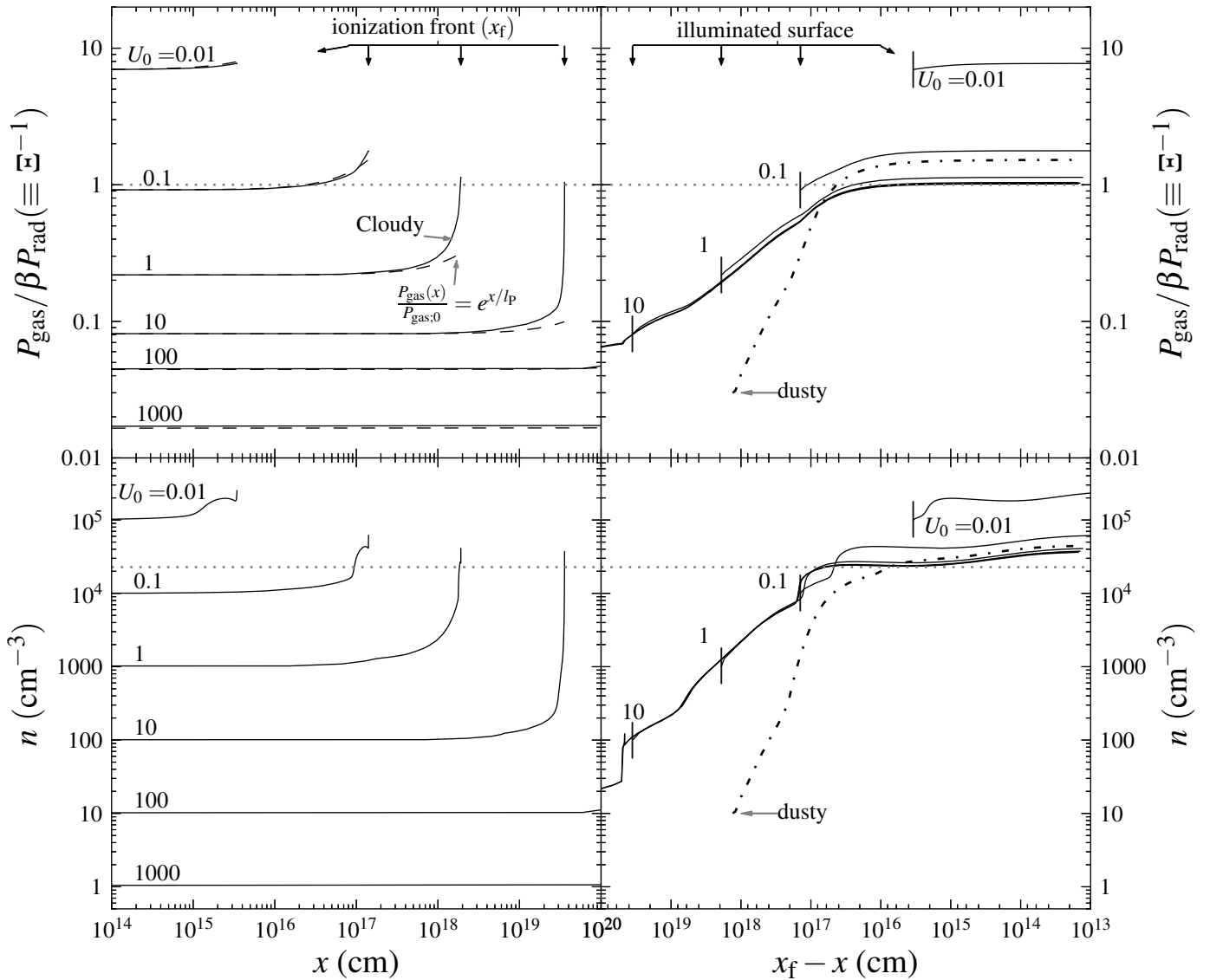


**Figure 4.** Same as Fig. 3, for dust-less models. **(Left panels)** Models with  $0.03 \ll U_0 \leq 10$  are RPC. With absorption of radiation,  $P_{\text{gas}}$  and  $n$  increase, reaching  $P_{\text{gas},f} = \beta P_{\text{rad}}$  and  $n_f \approx \beta P_{\text{rad}} / 2k_B \cdot 10^4$  (dotted horizontal lines), with  $\beta = 1.2$ . The  $l_P$  increases with  $U_0$ , due to the associated increase in  $T_0$  and the decrease in  $\bar{\sigma}_0$  (eq. 16). In models with  $U_0 \geq 100$ ,  $l_P > r \sim 70$  pc, and there is no significant increase in  $P_{\text{gas}}$  at  $x < r$ . **(Right panels)** As in the dusty models (Fig. 3), all dust-less models with  $U_0 \gg 0.03$  lie on the same  $P_{\text{gas}}(x_f - x)$  and  $n(x_f - x)$  profile. The dust-less models and the dusty model (dash-dotted lines) have a similar  $P_{\text{gas},f}$ , differing only due to their different  $\beta$ . The increase in  $n$  and  $P_{\text{gas}}$  in the surface layer of dust-less models occurs on scales 100 times larger than in the dusty models, mainly due to the lower  $\bar{\sigma}$ .

illuminated surface, where models with lower  $n_0$  extend to larger distances from the ionized front. Therefore, RPC models with different  $U_0$  have a very similar slab structure. Since most of the line emission comes from parts of the slab with  $n \lesssim n_f$  (see below), which Fig. 3 shows is common to all RPC solutions, it follows that RPC solutions are essentially independent of the boundary value  $n_0$  or  $U_0$ .

The right panels of Fig. 4 show that the dust-less models all lie on the same  $P_{\text{gas}}(x_f - x)$  and  $n(x_f - x)$  solution, as seen in the dusty models in Fig. 3. Therefore, our conclusion that the slab structure is insensitive to  $n_0$  is independent of the dust content of the gas. The effect of dust is apparent in two main aspects. The physical length of the optically thin surface layer is smaller by a factor of  $\sim 100$

in the dusty models, mainly due to the increase in  $\bar{\sigma}$ . Also,  $\beta$  and  $P_{\text{gas},f}$  are larger by 50% in the dusty models, due to the additional pressure from absorption of optical photons by the dust.

## 2.6 The slab structure vs. $n_\gamma$

For the assumed SED,

$$n_\gamma = 2040 \frac{L_{i,45} 36 \text{ eV}}{r_{50}^2 \langle h\nu \rangle} \text{ cm}^{-3} \quad (20)$$

How does the slab structure depend on  $n_\gamma$ ? or equivalently, for a given  $L_{\text{ion}}$ , how does the slab structure depend on  $r$ ?

At low  $n$ , the ionization state and  $T$  of the gas are a function

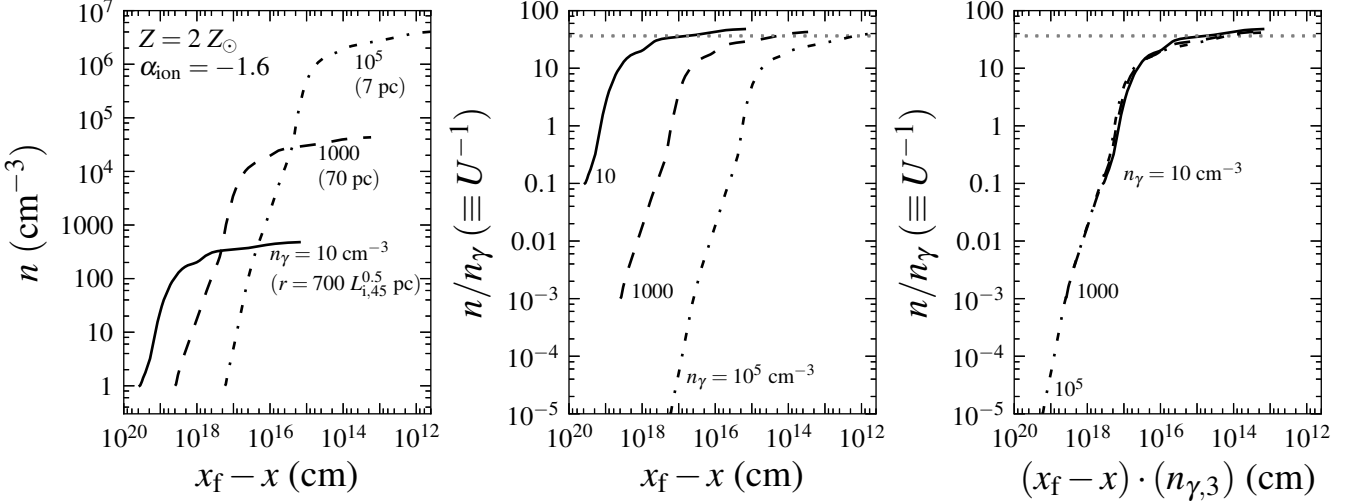


**Figure 5.** The density structure of RPC slabs with different  $n_\gamma$ . Each line denotes an RPC dusty model with a different  $n_\gamma$  (noted), or equivalently a different  $r$  (noted in left panel). Other model parameters are noted in the left panel. **(Left)** The  $n(x_f - x)$  profile. The  $n$  increases from the assumed  $n_0 = 1 \text{ cm}^{-3}$  to  $n_f \propto n_\gamma$ . **(Middle)** The ordinate is normalized by  $n_\gamma$ . All models reach the same  $U_f$  (eq. 7, dotted line). **(Right)** The ordinate is normalized by  $n_\gamma$  and the abscissa is normalized by  $(n_\gamma/1000 \text{ cm}^{-3})^{-1}$ . Models with different  $n_\gamma$  lie on the same  $n/n_\gamma$  vs.  $(x_f - x)n_\gamma$  profile. Therefore, the slab structure of RPC gas with different  $n_\gamma$  is similar if  $n$  is scaled by  $n_\gamma$  and  $x$  is scaled by  $n_\gamma^{-1}$ .

mainly of  $U$ , while the direct dependence on  $n$  and  $n_\gamma$  are only a second-order effect. This insensitivity of the ionization state to  $n$  and  $n_\gamma$  follows from the fact that the ionization rate is  $\propto n_\gamma n$ , while the recombination rate is  $\propto n^2$ . Therefore the ionization balance is mainly a function of  $n_\gamma/n \equiv U$ . Similarly, the heating rate depends on  $n_\gamma \langle h\nu \rangle n$ , while collisional cooling is  $\propto n^2$ . Hence, for a given SED the  $T$  balance is also determined to first order by  $U^3$ .

The above reasoning assumes a fixed dust content in the gas, since a changing dust content with  $n_\gamma$  will create a direct relation between the slab structure and  $n_\gamma$ . This assumption is violated at  $10^{5.9} < n_\gamma < 10^{8.6} \text{ cm}^{-3}$ , where different dust grain species sublimate at different  $n_\gamma$  (§4).

To understand the effect of  $n_\gamma$  on the slab structure, we examine its effect on  $l_p$ , which determines the physical scale of the slab. Eq. 17 shows that the value of  $l_p \cdot n_\gamma$  depends on  $\beta$ ,  $T$ ,  $\langle h\nu \rangle$  and  $\bar{\sigma}$ . The reasoning above implies that  $T$  is a function of  $U$ . The values of  $\bar{\sigma}$  and  $\beta$  depend on the ionization state,  $T$ , and dust content of the gas, and are therefore also mainly a function of  $U$  at  $n_\gamma < 10^{5.9} \text{ cm}^{-3}$ . Hence, for a given  $\langle h\nu \rangle$  we can write

$$l_p n_\gamma = \mathcal{F}(U) = \mathcal{F}\left(\frac{n_\gamma}{n}\right) \quad (21)$$

where  $\mathcal{F}(U)$  is a computable function of  $U$ . Eq. 21 suggests that solutions of models with different  $n_\gamma$  are equivalent, if we scale  $n$  by  $n_\gamma$ , and scale  $x$  by  $n_\gamma^{-1}$ .

In Figure 5, we show the validity of eq. 21 using CLOUDY calculations. The left panel shows  $n$  vs.  $x_f - x$  of dusty RPC slabs with different values of  $n_\gamma$ . We assume  $n_0 = 1 \text{ cm}^{-3}$  in all models. The value of  $n$  increases as radiation pressure is absorbed, reaching a  $n_f$  which increases with increasing  $n_\gamma$ . In the middle panel  $n$  is scaled by  $n_\gamma$ . All models reach the same  $n_f/n_\gamma$ , as expected from eq. 7. In the right panel we also scaled  $(x_f - x)$  by  $n_\gamma^{-1}$ . The  $U$  vs.  $(x_f - x)n_\gamma$  profiles of the different models are almost identical, as

implied by eq. 21. The models differ only in the starting point of their solution, due to the different assumed  $U_0$ . Therefore, the slab structure of dusty RPC models with different  $n_\gamma$  are similar once  $x$  is scaled by  $n_\gamma^{-1}$  and  $n$  is scaled by  $n_\gamma$ . Dust-less RPC models with different  $n_\gamma$  show the same property, as do RPC models of warm absorbers (Chevallier et al. 2007).

We can now derive the range in  $r$  where the slab approximation ( $x_f \ll r$ ) is valid. Since  $P_{\text{gas}}$  increases exponentially with a scale of  $l_p$  (eq. 14), and since the largest  $l_p$  is at the surface, then  $x_f \lesssim \ln(n_f/n_0) \cdot l_{p,0}$ . We assume  $U_0 = 100$ , as material at higher  $U$  does not emit emission lines, so from eq. 7 we get  $\ln(n_f/n_0) = \ln(U_0/U_f) = 8$ . In the dusty  $n_\gamma = 1000 \text{ cm}^{-3}$  model we find  $\bar{\sigma}_{-21} = 1.6$ ,  $T_6 = 0.7$  and  $\beta = 1.9$  at the surface. The above discussion suggests that these properties are independent of  $r$ . Therefore, by plugging these values in eq. 16 we get

$$\frac{x_{f,\text{dusty}}}{r} \lesssim \frac{8 l_{p,0}}{r} = 0.03 L_{1,45}^{-1} r_{50} \quad (22)$$

implying that in dusty RPC gas the slab approximation is valid at least up to kpc scale. In contrast, at the surface of the  $U_0 = 100$  dust-less model we find  $\bar{\sigma} = \bar{\sigma}_{\text{es}}$ ,  $T_6 = 1$  and  $\beta = 2.9$ , so

$$\frac{x_{f,\text{dust-less}}}{r} \lesssim \frac{8 l_{p,0}}{r} = 55 L_{1,45}^{-1} r_{50} \quad (23)$$

implying that the slab approximation is invalid for dust-less gas on NLR scales, if  $U_0 = 100$ . The right panels of Fig. 4 show that at  $r = 70 L_{1,45} \text{ pc}$ , the slab approximation will be valid only if  $U_0 < 10$ .

## 2.7 Emission line emissivity vs. $r$

In the previous sections, we showed that RPC slabs have  $n \propto r^{-2}$ . In this section, we use this result to predict the emission line luminosities  $L_{\text{line}}$  as a function of  $r$ .

To calculate  $L_{\text{line}}$ , we use CLOUDY, as described in §2.4.2. We run a grid of dusty CLOUDY models with  $n_\gamma = 10^{-1.5} - 10^8 \text{ cm}^{-3}$ , which corresponds to  $r = 0.2 - 10^4 L_{1,45}^{1/2} \text{ pc}$  (eq. 20). We set  $U_0 = 10^4$ , to reside deep in the RPC regime. Identical results are

<sup>3</sup> A notable exception is Compton cooling, which is  $\propto n_\gamma \langle h\nu \rangle n$ . In this case the  $T$  balance is independent of either  $n$ ,  $n_\gamma$  or  $U$ , and determined solely by the SED.



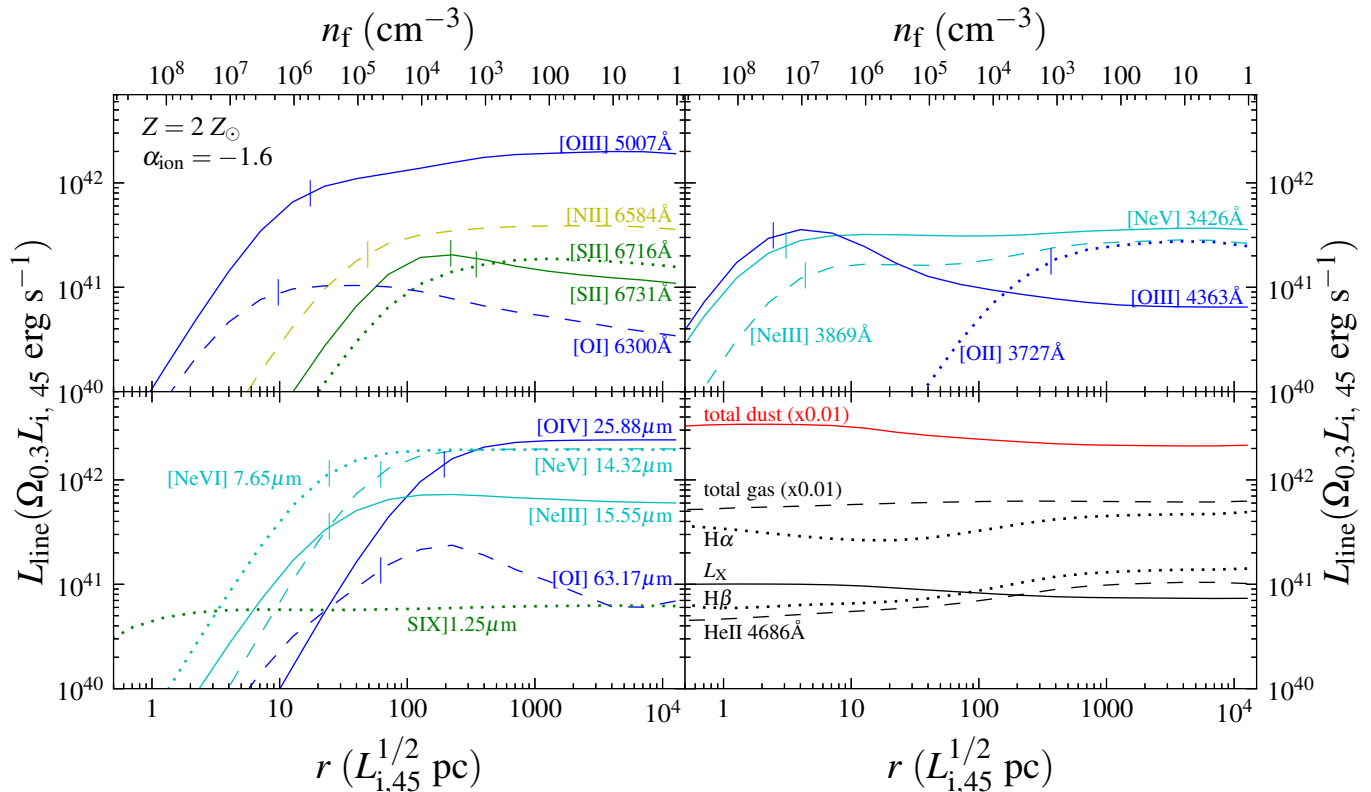


**Figure 6.** The emission line luminosity of RPC slabs, vs. distance from the nucleus. Plotted lines denote  $L_{\text{line}}$  at different  $r$ , for  $L_{i,45} = 1$  and a covering factor  $\Omega(r) = 0.3$ . The  $L_{\text{line}}$  are calculated by CLOUDY using dusty gas and the model parameters noted in the top-left panel. The line marked ‘ $L_X$ ’ includes all line emission at 0.5–2keV. Also shown are the total emission from the dust grains and the total emission from the gas, scaled down by a factor of 100 (lower right panel). The  $n_f$  (noted on top) is set by  $r$  via eq. 6. The approximate EW of an optical line with wavelength  $\lambda$  can be derived by dividing the y-axis value by  $6.1 \times 10^{40} (\lambda/5007\text{\AA})^{-1.5} \text{erg s}^{-1} \text{\AA}^{-1}$ . A wide range of gas ionization states is observed at each  $r$ , from [O I]-emitting layers to S IX. The  $L_{\text{line}}$  of recombination lines, and the total gas and dust luminosities, are constant with  $r$  up to a factor of  $\sim 2$ , due to the similar slab structure at different  $r$  (Fig. 5). The  $n_{\text{crit}}$  of forbidden lines are marked by ‘|’. At  $n_f \gg n_{\text{crit}}$ , forbidden lines exhibit  $L_{\text{line}} \propto n_f^{-1} \propto r^{-2}$  due to collisional de-excitation. At  $n_f \ll n_{\text{crit}}$ , forbidden lines exhibit radial dependencies between  $L_{\text{line}} \propto r^{-0.6}$  and  $L_{\text{line}} \propto r^0$ .

found for all  $U_0 \geq 1$ , as implied by Fig. 3. We set  $Z = 2Z_{\odot}$  and  $\alpha_{\text{ion}} = -1.6$  (see §2.4.2). Our choice of a dusty model is motivated by the observations that the emission line gas is likely dusty at  $n_{\gamma} < 10^{8.5} \text{cm}^{-3}$ , at least in layers which emit emission lines with IP  $\sim 40\text{eV}$  or less (§4). The plotted  $L_{\text{line}}$  of lines with IP  $\gg 40\text{eV}$  may be inaccurate if dust is significantly destroyed in the layers in which they are emitted. Also, we disregard the change in dust composition due to sublimation of small grains at  $10^{5.9} < n_{\gamma} < 10^{8.5} \text{cm}^{-3}$  (see §4.1.1). Since we assume the slab is semi-infinite, all emission properties are measured at the illuminated surface. The back side of the slab should mainly emit dust thermal IR emission.

The value of  $L_{\text{line}}$  of different emission lines for different  $r$  are shown in Figure 6. We mark the sum of emission of lines with energies 0.5–2keV by  $L_X^4$  (lower right panel). Also shown are the total emission from the dust grains and the total emission from the gas. We assume  $L_{i,45} = 1$ , and a covering factor at  $r$ ,  $\Omega(r)$ , of 0.3. The  $L_{\text{line}}(r)$  for other values of  $L_{i,45}$  and  $\Omega(r)$  can be derived with the appropriate scaling. The approximate equivalent width (EW) of

an optical line with wavelength  $\lambda$  can be derived by dividing the y-axis value by  $6.1 \times 10^{40} (\lambda/5007\text{\AA})^{-1.5} \text{erg s}^{-1} \text{\AA}^{-1}$ .

Several properties of the emitted spectrum can be deduced from Fig. 6. Emission lines from a wide range of ionization states are apparent, from the coronal and soft X-ray lines emitted from the surface layer, to the [S II] and [O I] lines emitted from the partially ionized layer. The luminosities of all shown recombination lines, and the total gas and dust luminosities (lower right panel), are constant with  $r$  up to a factor of  $\sim 2$ . This similarity is due to the similar slab structure at different  $r$  (Fig. 5), and because these emission properties are independent of  $n$ . The fraction of emission in dust IR thermal emission is 77-87%. This high fraction is because in RPC, most of the absorption occurs at  $U > U_f = 0.03$  (eq. 7), where dust dominates the opacity. The dominant trend with decreasing  $r$  is the collisional de-excitation of forbidden lines. At  $n_f \gg n_{\text{crit}}$ ,  $L_{\text{line}} \propto n_f^{-1} \propto r^2$ . The luminosities of [O III] 4363Å, [O I] 6300Å and [O I] 63.17μm peak at  $n_f \sim n_{\text{crit}}$ , while the luminosities of most other forbidden lines actually remains constant at  $n_f \ll n_{\text{crit}}$ .

Weaker trends include the decrease in Hβ and He II 4686Å by a factor of two with decreasing  $r$ . This decrease is because  $T$  increases at lower  $r$ , due to the collisional suppression of the main coolants. The increase in  $T$  induces a higher  $U$  (see eq. 7), which in-

<sup>4</sup> The  $L_X$  is dominated by recombination and resonance lines, as expected for photoionized gas.

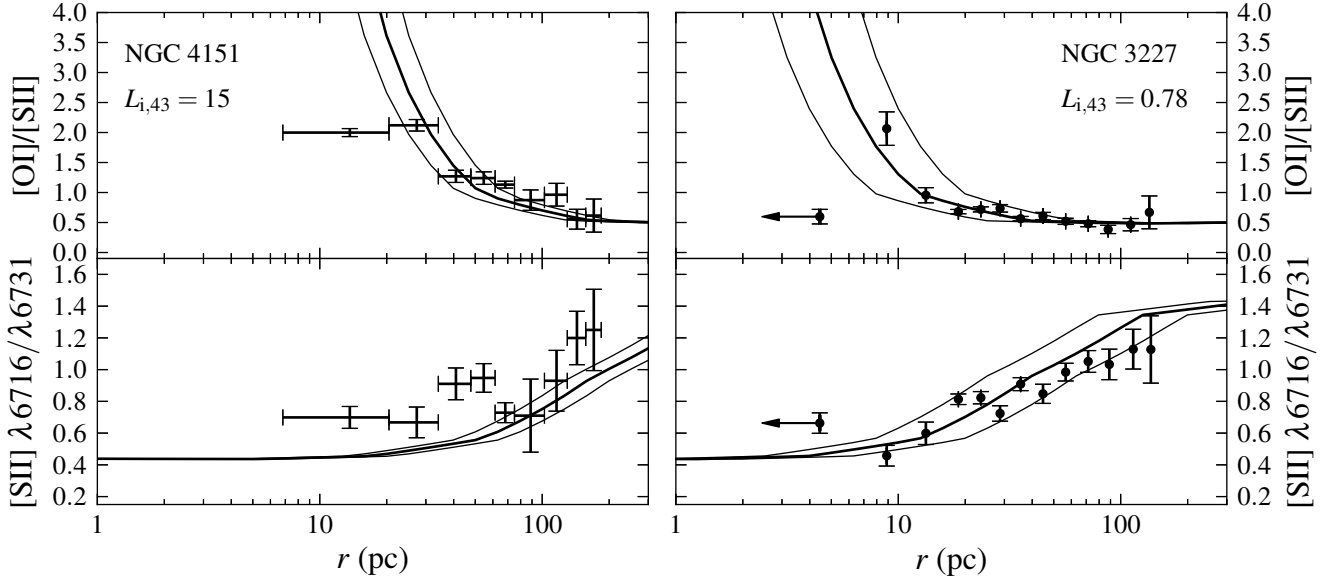


**Figure 7.** The expected and observed NLR gas density as a function of distance. The error bars are *HST* observations of the  $n_f$ -sensitive [O I]/[S II] and [S II]  $\lambda 6716/\lambda 6731$  ratios from Kraemer et al. (2000a, NGC 4151, left panels) and from Walsh et al. (2008, NGC 3227, right panels). The center measurement in NGC 3227 is marked by a left-pointing arrow. The black solid line in each panel plots the expected line ratios for RPC slabs at different  $r$ . The calculations are performed with CLOUDY, with no free parameters. The gray lines denote the uncertainty due to the assumed 0.2 dex uncertainty in the  $L_{\text{ion}}$  estimate, which is noted in the top panels. Except the central measurement, the observed [O I]/[S II] ratios agree with the RPC calculations. In NGC 4151, the expected  $\lambda 6716/\lambda 6731$  are typically lower than observed. In NGC 3227, the observed  $\lambda 6716/\lambda 6731$  imply a somewhat flatter  $n_f$  vs.  $r$  relation than expected by RPC. We suspect that since  $\lambda 6716/\lambda 6731$  is sensitive only to a small dynamical range in  $n$ , projection effects in the observations may hinder the ability of  $\lambda 6716/\lambda 6731$  to estimate the true  $n_f$  at each  $r$ .

creases the ratio of dust to gas opacity, thus decreasing the amount of ionizing photons absorbed by H and He. This trend disappears in the dust-less models, where the emissivity of recombination lines remains constant with  $r$ . However, the model ignores sublimation of the smaller grains at small  $r$ , which will decrease the dust to gas opacity compared to large  $r$ , and will affect the line strength.

We note that RPC implies that one cannot define a boundary between the so-called ‘torus’ and the NLR. The lower right panel of Fig. 6 shows that the dust IR thermal emission per unit  $\Omega$  is nearly the same on ‘torus scales’ (immediately beyond the sublimation radius) and on ‘NLR scales’ (10 pc – 1 kpc). Both thermal IR dust emission and recombination lines are emitted at all  $r$ , with a nearly constant emissivity per unit  $\Omega$ . Only specific forbidden lines cannot be emitted at small enough  $r$ , depending on their  $n_{\text{crit}}$ , due to collisional de-excitation.

Below, we compare the results of Fig. 6 with both resolved and unresolved observations of the NLR. In order to compare RPC with unresolved observations, we need to know  $\Omega(r)$ , in order to derive the value of  $L_{\text{line}}$  integrated over all  $r$ . For simplicity, we parameterize  $\Omega(r)$  as a power-law:

$$\frac{d\Omega(r)}{d\log r} \propto r^\eta \quad (r_{\text{in}} < r < r_{\text{out}}) \quad (24)$$

Now, the emissivity of forbidden lines scales as  $r^2$  at  $n \gg n_{\text{crit}}$ , and is constant or decreasing with  $r$  at  $n \ll n_{\text{crit}}$  (Fig. 6). Therefore, eq. 24 implies that if  $-2 < \eta < 0$ , then the integrated  $L_{\text{line}}$  will be dominated by emission from  $r$  such that  $n_f(r) \sim n_{\text{crit}}$ .

A constraint on  $\eta$  can be derived from the flat IR  $\nu L_\nu$  slope observed in quasars at  $10^{13} < \nu < 10^{14}$  Hz (e.g. Richards et al. 2006). This flat slope suggests that the dust thermal emission per unit log  $T_{\text{dust}}$  is constant at  $100\text{K} < T_{\text{dust}} < 1000\text{K}$ . To first or-

der,  $T_{\text{dust}}$  is proportional to the effective temperature of the radiation (see fig. 8 in Laor & Draine 1993), which is  $\propto r^{-1/2}$ . The emission at each  $r$  is  $\propto d\Omega(r)$ . Therefore, the flat IR slope implies  $d\Omega(r)/d(\log r^{-1/2}) \propto r^0$ . Using the definition of  $\eta$ , this relation implies that  $\eta \sim 0$ , at  $r$  where  $T_{\text{dust}}(r) > 100\text{K}$ .

### 3 COMPARISON WITH OBSERVATIONS

RPC provides robust predictions on the gas properties as a function of distance in AGN. Are these properties observed?

#### 3.1 Resolved observations of the $n_f$ vs. $r$ relation

We compare eq. 6 with *HST* observations of two Seyferts in the literature, NGC 4151 which was observed by Kraemer et al. (2000), and NGC 3227 which was observed by Walsh et al. (2008). To estimate  $L_{\text{ion}}$ , we use the Laor (2003) bolometric luminosity ( $L_{\text{bol}}$ ) estimates, which are based on the Ho & Peng (2001) B-band nuclear magnitude measurements taken by *HST*. In order to estimate the observed  $n_f$ , we use the [O I]  $\lambda 6300$ /[S II]  $\lambda 6716$  ratio (e.g. Barth et al. 2001). These two low ionization lines are both emitted from the partially ionized region of the slab, where  $n \sim n_f$ . However, because these lines differ significantly in  $n_{\text{crit}}$ , their luminosity ratio is sensitive to  $n$  at  $10^{2.5} \lesssim n \lesssim 10^{6.5} \text{cm}^{-3}$  (Fig. 6). We use models with  $Z = 2Z_\odot$  and  $\alpha_{\text{ion}} = -1.4$ , typical of AGN with Seyfert luminosities (Steffen et al. 2006). We set  $L_{\text{ion}} = 0.35 L_{\text{bol}}$ , appropriate for our assumed SED. We find  $L_{i,43} = 15$  and  $L_{i,43} = 0.78$  for NGC 4151 and NGC 3227, respectively, where  $L_{\text{ion}} = 10^{43} L_{i,43} \text{erg s}^{-1}$ . We assume an error of 0.2 dex in the  $L_{\text{ion}}$  estimate. Walsh et al. (2008) also observed [O I] in four LINERs

(Heckman 1980), though the incident SED and  $L_{\text{ion}}$  are not well-constrained in LINERs, so a quantitative comparison with RPC is less reliable. We discuss LINERs in the context of RPC in §5.

The expected and observed [O I]/[S II] are compared in the top panels of Figure 7. In NGC 4151, we average the observations of the South-West and North-East sides of the slit. In NGC 3227, we average over all position angles in bins of 0.1 dex in  $r$ . We note that the central measurement in NGC 3227 is somewhat uncertain due to spectral decomposition issues, and due to geometric rectification issues during the data reduction (J. Walsh, private communication). Except the central measurement, the observed [O I]/[S II] agree with the RPC calculations. We emphasize that there are no free parameters in the RPC model calculations presented in Fig. 7.

The [S II] doublet is commonly used to measure  $n$  (e.g. Walsh et al. 2008). In the lower panels of Fig. 7, we compare the observed ratios of the [S II] doublet with the RPC calculation. In NGC 3227, the observed [S II] ratio vs.  $r$  relation is somewhat flatter than expected from RPC, and in NGC 4151, the observed [S II] ratios are typically higher than expected. Kraemer et al. (2000) found a similar discrepancy between the observed [S II] ratios and the  $n$  required by the other emission lines (see their figs. 4 and 7). The [S II] ratio is sensitive to  $n$  only at  $10^2 < n < 10^4 \text{ cm}^{-3}$ , half the dynamical range which can be probed by [O I]/[S II]. Therefore, the observed [S II] ratio will be more sensitive to projection effects of emission from gas on larger scales, which may explain the discrepancy.

### 3.2 Forbidden line profiles

In §2.7 we showed that if  $-2 < \eta < 0$ , the emission of a forbidden line will be dominated by gas which resides at  $r$  such that  $n_f(r) \sim n_{\text{crit}}$ . Since  $n_f \propto r^{-2}$ , we expect the line profile of forbidden lines with high enough  $n_{\text{crit}}$  to be dominated by gas at  $r < r_{\text{inf}}$ , where  $r_{\text{inf}}$  is the gravitational radius of influence of the black hole. Such emission lines are expected to show an increase of profile width with  $n_{\text{crit}}$ . In contrast, a constant width is expected from lower  $n_{\text{crit}}$  lines, which originate at  $r > r_{\text{inf}}$  where the gas kinematics are dominated by the bulge (Filippenko & Sargent 1988; Laor 2003). In this section, we show that RPC and the  $-2 < \eta < 0$  assumption is consistent with the observed widths of high  $n_{\text{crit}}$  forbidden lines in AGN.

At  $r > r_{\text{inf}}$ , we expect the emission line profile to be determined by the stellar velocity dispersion,  $\sigma_*$ . Therefore, for a Gaussian profile the Full Width Half Max ( $\nu$ ) is  $2.35\sigma_*$ . At  $r < r_{\text{inf}}$ , assuming Keplerian motion and neglecting projection effects (see Laor 2003), we expect  $\nu^2 = GM_{\text{BH}}/r$ , where  $M_{\text{BH}}$  is the black hole mass. Therefore,  $r_{\text{inf}}$  can be derived from:

$$\sqrt{\frac{GM_{\text{BH}}}{r_{\text{inf}}}} = 2.35\sigma_* \quad (25)$$

Using  $\sigma_*/200 \text{ km s}^{-1} = (M_{\text{BH}}/10^{8.12} M_{\odot})^{1/4.24}$  from Gültekin et al. (2009), we get

$$r_{\text{inf}} = \frac{GM_{\text{BH}}}{5.5\sigma_*^2} = 2.3 M_{\text{BH},8}^{1/2} \text{ pc} \quad (26)$$

where  $M_{\text{BH}} = 10^8 M_{\text{BH},8} M_{\odot}$ . Therefore, from eqs. 6 and 26

$$n_f(r_{\text{inf}}) = 1.6 \times 10^8 \dot{m} T_{f,4}^{-1} \text{ cm}^{-3} \quad (27)$$

where  $\dot{m}$  is  $L_{\text{bol}}$  in units of the Eddington luminosity, and we set  $L_{\text{ion}} = 0.35 L_{\text{bol}}$ , as above. At  $r < r_{\text{inf}}$ , we assume  $\nu$  is dominated

Object	$M_{\text{BH}}$	$L_{i,43}$	$\sigma_*$	Ref.	estimated $M_{\text{BH}}$
M 81	7.8	0.01	143	5	6.8
PKS 1718-649	8.5	0.3	243	2	8.0
NGC 7213	8.0	0.6	185	1	8.2
Pictor A	7.5	2	145	2	7.9
NGC 3783	6.9	3	105	3	7.4
Ark 120	8.4	60	239	3	8.4
MR 2251-178	8.1	100	196	2	8.4
PG 2251+113	8.9	900	311	4	9.5

**Table 1.** Properties of the objects in Fig. 8, compiled from the literature. The  $M_{\text{BH}}$ ,  $L_{\text{ion}}$ , and  $\sigma_*$  are given in units of  $\log M_{\odot}$ ,  $10^{43} \text{ erg s}^{-1}$  and  $\text{km s}^{-1}$ , respectively. The references for the NLR  $\nu$  measurements are: 1. Filippenko & Halpern (1984) 2. Filippenko (1985) 3. Appenzeller & Oestreich (1988) 4. Espey et al. (1994) 5. Ho et al. (1996). The estimate of  $M_{\text{BH}}$  based on RPC is described in §5.4.

by emission from  $r$  such that  $n_f(r) = n_{\text{crit}}$ . Using eq. 6 with  $T_{f,4} = 1$  we get

$$\nu = \sqrt{\frac{GM_{\text{BH}}}{r(n_{\text{crit}})}} = 570 M_{\text{BH},8}^{1/2} L_{i,43}^{-1/4} n_{\text{crit},6}^{1/4} \text{ km s}^{-1} \quad (28)$$

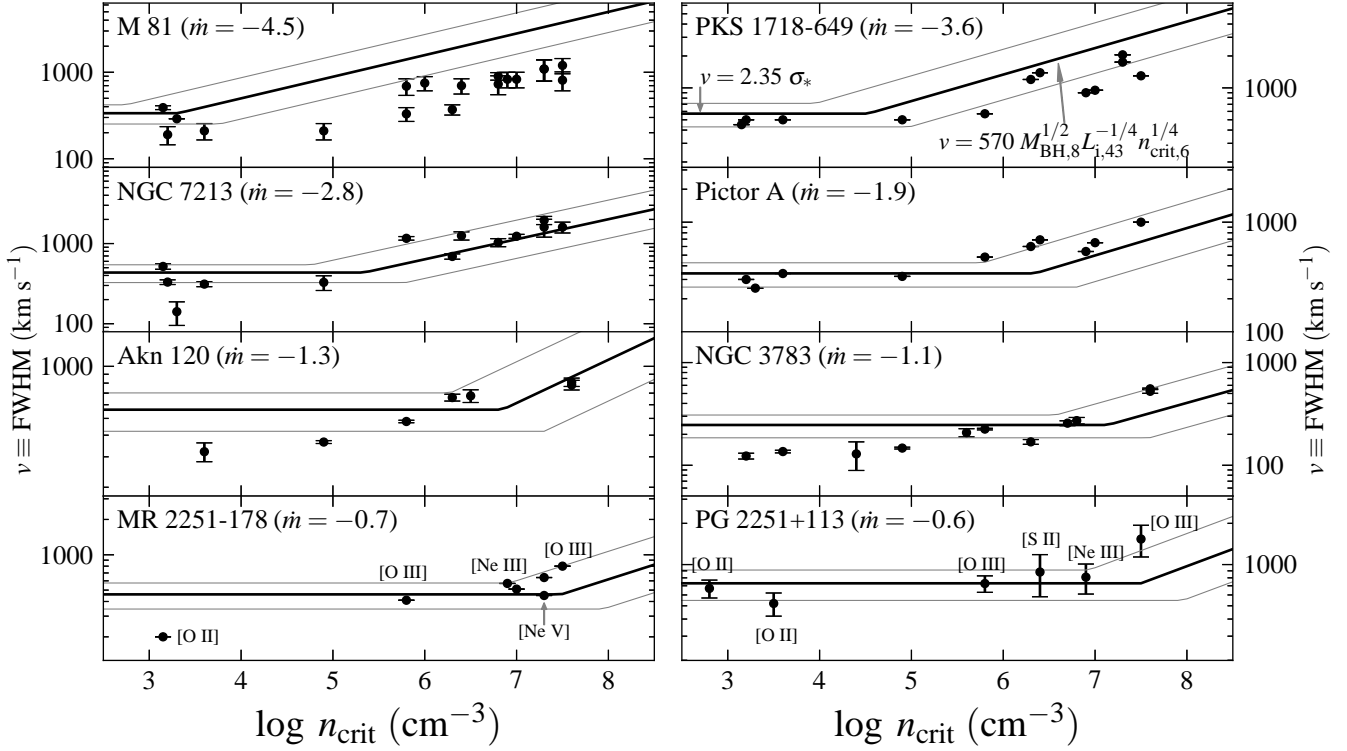
Fig. 1 shows  $r_{\text{inf}}$  for  $M_{\text{BH},8} = 1$ . The  $M_{\text{BH}}$  will increase the width of an emission line if the intersection of the appropriate  $n_{\text{crit}}$  (dotted line) with the appropriate  $L_{\text{ion}}$  (solid line) are at  $r < r_{\text{inf}}$ . For example, [O III]  $\lambda 4363$  ( $n_{\text{crit}} = 10^{7.5} \text{ cm}^{-3}$ ) will be emitted at  $r < r_{\text{inf}}$  in  $\dot{m} < 0.2$  AGN, while [O III]  $\lambda 5007$  ( $n_{\text{crit}} = 10^{5.8} \text{ cm}^{-3}$ ) will have emission from  $r < r_{\text{inf}}$  if  $\dot{m} < 10^{-2.5}$ .

Figure 8 compares the observed  $\nu$  vs.  $n_{\text{crit}}$  with eq. 28, for the seven type 1 AGN with measurements of  $\nu$  listed in Espey et al. (1994). We add also M 81, which has measurements of  $\nu$  of 18 forbidden lines in Ho et al. (1996). We avoid type 2 AGN where high  $n$  gas near the nucleus may be obscured. The estimates of  $M_{\text{BH}}$ ,  $L_{\text{ion}}$ , and  $\sigma_*$  for the different objects are gathered from the literature, as detailed in Appendix B. They are listed in Table 1, together with the references for the  $\nu$  measurements. We assume a factor of three uncertainty in the  $M_{\text{BH}}$  estimates, and an uncertainty of 25% in the  $\sigma_*$  estimates. The uncertainty in  $L_{\text{ion}}$  in the Seyferts is small compared to the uncertainty in the  $M_{\text{BH}}$  estimate, however the estimate of  $L_{\text{ion}}$  in the LINERs (M 81, PKS 1716-649 and NGC 7213) is highly uncertain.

Note that some of the emission lines in Fig. 8 have high IP, implying that they are emitted from a layer in the slab in which  $n < n_f$ . The highest IP lines shown, [Ne V] and [Fe VII] (IP= 97 eV), have an emissivity averaged  $n \approx 0.1 n_f$  in our CLOUDY models. Therefore, the  $r$  where  $n = n_{\text{crit}}$  in these lines is smaller by a factor of  $0.1^{1/2}$  than the  $r$  derived assuming  $n_f = n_{\text{crit}}$ . Hence, the observed  $\nu$  is expected to be larger by a factor of  $\sim 0.1^{-1/4}$  than expected from eq. 28. For simplicity, and due to the uncertainties induced by the unknown  $\Omega(r)$  distribution, the assumption of Keplerian motion, and possible projection effects, we do not incorporate this additional complication in our calculations.

The objects in Fig. 8 span a dynamical range of  $10^4$  in  $\dot{m}$ . With increasing  $\dot{m}$ , there is a clear increase in the observed  $n_{\text{crit}}$  where the  $\nu$  rises above  $2.35\sigma_*$ , as expected from eq. 27. The slope of the observed relation between  $\nu$  and  $n_{\text{crit}}$  at  $n_{\text{crit}} > n_{\text{crit}}(r_{\text{inf}})$  is consistent with 1/4, as expected from eq. 28. With the exception of M 81, the actual observed  $\nu$  are generally consistent with eq. 28 and the  $M_{\text{BH}}$  and  $L_{\text{ion}}$  estimates. Therefore, the gas at  $r < r_{\text{inf}}$  is likely RPC. We emphasize again that there are no free parameters in the RPC results.

It is also possible to estimate  $\nu(n_{\text{crit}})$  directly from the FWHM



**Figure 8.** The relation between line width and  $n_{\text{crit}}$  implied by RPC, compared to observations of type 1 AGN. The solid line in each panel denotes the expected  $v(n_{\text{crit}})$ , with no free parameters. The relation is flat at  $n_{\text{crit}} < n_{\text{crit}}(r_{\text{inf}})$  where the bulge dominates the gas kinematics, and has a slope of 1/4 at  $n_{\text{crit}} > n_{\text{crit}}(r_{\text{inf}})$ , where the kinematics are dominated by the black hole (eq. 28). The  $n_{\text{crit}}(r_{\text{inf}})$  depends on  $\dot{m}$  (eq. 27), which is noted in each panel. The normalization at  $n > n_{\text{crit}}(r_{\text{inf}})$  is based on estimates of  $M_{\text{BH}}$  and  $L_{\text{ion}}$  taken from the literature, with a factor of three error assumed on the  $M_{\text{BH}}$  estimates (gray lines). The error bars denote the observed  $v$  of different forbidden emission lines, from the references listed in Table 1. Some line designations are noted in the lower panels. With increasing  $\dot{m}$ , there is a clear increase in the lowest observed  $n_{\text{crit}}$  where the  $v$  rises above  $2.35\sigma_*$ , as expected from RPC. The observed  $v(n_{\text{crit}})$  relation is generally consistent with the slope and normalization implied by RPC. Therefore, the gas at  $r < r_{\text{inf}}$  is likely RPC.

of the broad  $\text{H}\alpha$ ,  $v_{\text{BLR}}$ , with no relation to the value of  $M_{\text{BH}}$ . In a single object, the low ionization part of the BLR appears to be dominated by gas from a small range of  $r$ , which satisfies  $r_{\text{BLR}} \propto L_{1450\text{\AA}}^{0.55}$  (Kaspi et al. 2005). Therefore, assuming a Keplerian velocity field and using the Kaspi et al. relation, we get

$$\frac{v(n_{\text{crit}})}{v_{\text{BLR}}} = \left( \frac{r(n_{\text{crit}})}{r_{\text{BLR}}} \right)^{-1/2} = \left( \frac{1.4 n_{\text{crit},6}^{-1/2} L_{i,43}^{1/2} \text{pc}}{0.0036 L_{i,43}^{-1/2} \text{pc}} \right)^{-1/2} = 0.05 n_{\text{crit},6}^{1/4} \quad (29)$$

where we assumed  $L_{\text{bol}}/L_{1450\text{\AA}} = 4$  (Richards et al. 2006).

### 3.3 Emission line ratios: high IP vs. low IP

The RPC slab structure seen in Figs. 2–5 implies a highly ionized surface followed by a less ionized inner layer. Hence, in RPC gas the high IP and low IP emission lines come from the same slab, and their expected emissivity ratios can be calculated. This predictability is distinct from other models, such as locally-optimal emitting clouds (Ferguson et al. 1997), where lines with different IP come from different slabs, and therefore their emission ratios are not constrained.

G04 and Gorjian et al. (2007) showed that the observed unresolved  $[\text{Ne V}] 3426\text{\AA}/[\text{Ne III}] 3869\text{\AA}$  and  $[\text{Ne V}] 14.32\mu\text{m}/[\text{Ne III}] 15.55\mu\text{m}$  are generally consistent with dusty RPC models with  $n_{\text{f}} = 1000\text{cm}^{-3}$ . We extend their

analysis, by comparing observed emission line ratios from well defined samples, with RPC models with  $n_{\text{f}}$  in the range  $30 - 3 \times 10^7\text{cm}^{-3}$ . Also, we compare the RPC calculations with resolved observations.

#### 3.3.1 Unresolved observations

We choose emission line couples according to the following guidelines:

- (i) The lines differ in IP, so the luminosity ratio is sensitive to the relative emission from different layers in the slab.
- (ii) Strong emission, so the emission lines are observable with high S/N.
- (iii) The lines have similar  $n_{\text{crit}}$ , to reduce the dependence of the luminosity ratio on the unknown  $\Omega(r)$ .
- (iv) The lines are weak in star forming regions, to avoid contamination from other sources.
- (v) The lines are not blended with broad lines or stellar absorption features, so the reliability of the measurements is high.
- (vi) Lines from a noble element are preferred, so the luminosity is not directly sensitive to depletion.

The chosen couples are the optical  $[\text{Ne V}] 3426\text{\AA}/[\text{O III}] 5007\text{\AA}$  and  $[\text{O III}] 5007\text{\AA}/[\text{O I}] 6300\text{\AA}$ , and the IR  $[\text{Ne VI}] 7.652\mu\text{m}/[\text{Ne III}] 15.55\mu\text{m}$  and  $[\text{Ne V}] 14.32\mu\text{m}/[\text{Ne III}] 15.55\mu\text{m}$ . The differences in  $n_{\text{crit}}$



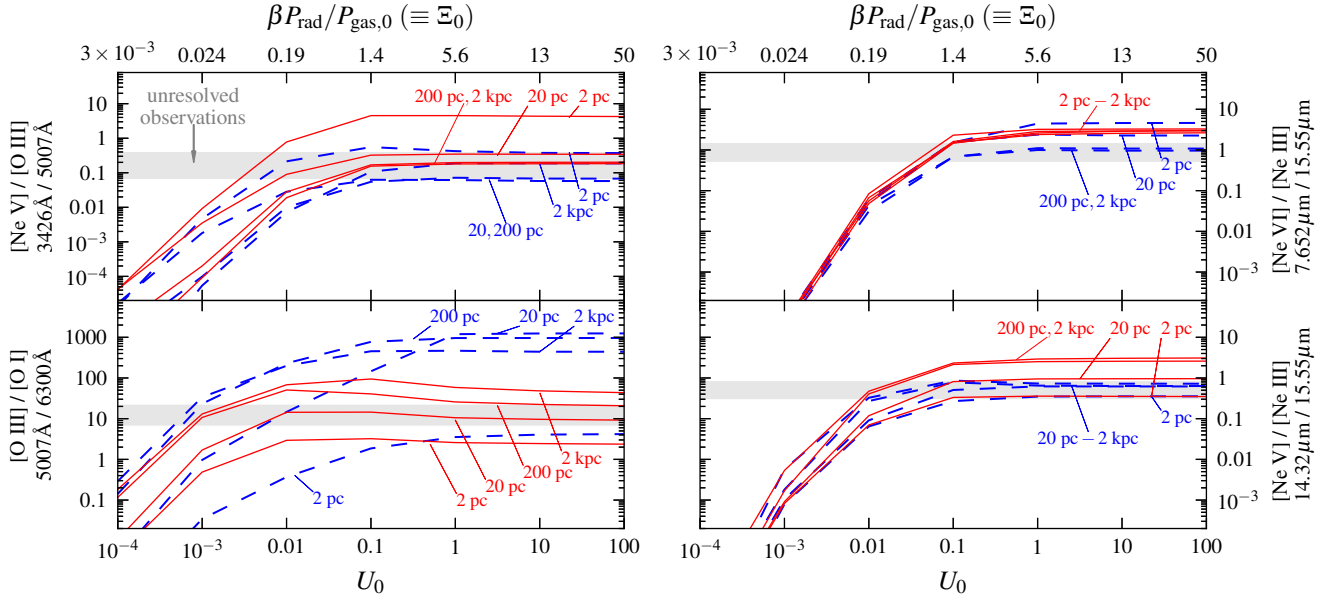


**Figure 9.** Expected vs. observed high ionization to low ionization emission line ratios. In each panel, the four solid red lines represent dusty models with  $Z = 2Z_{\odot}$ ,  $\alpha_{\text{ion}} = -1.6$  and  $r = 2 - 2000 L_{1.45}^{1/2}$  pc. The four dashed blue lines represent dust-less models with the same parameters. For each  $r$ , models are calculated for a range of  $U_0$ , or equivalently, a range in  $\Xi_0$  (noted on top). Models with  $U_0 \gg 0.03$  ( $\Xi_0 \gg 1$ ) are RPC, and their emission line ratios are independent of  $U_0$ . Models with lower  $U_0$  require an additional confinement source which is stronger than RPC. Gray stripes show the one-sigma range of emission line ratios in unresolvable observations of luminous type 1 AGN. The observed ratios are consistent with the RPC calculation to within a factor of 2–3, and rule out a significant contribution to these emission lines from slabs with  $U_0 \ll 0.03$ . The observed [O III]/[O I] suggests that the layer which emits these lines is dusty.

of these four couples are 1.5, 0.5, 0. dex, and 0.8 dex, respectively. The IPs are 0, 35, 41, 97 and 126 eV, for [O I], [O III], [Ne III], [Ne v], and [Ne VI], respectively. We use emission line observations of luminous type 1 AGN with well-defined selection criteria, as detailed in Appendix C. Type 1 AGN are preferred since the narrow line ratios are not part of the selection process, and reddening effects should be less severe than in type 2 AGN.

The predicted emission line luminosity ratios are calculated with CLOUDY (§2.4.2), using dusty and dust-less models with  $\alpha_{\text{ion}} = -1.6$ ,  $Z = 2Z_{\odot}$  and  $r$  in the range  $2 - 2000 L_{1.45}^{1/2}$  pc. The observed emission in each object is expected to be a weighted sum of the emission from slabs at different  $r$ . To emphasize the effect of RPC, we vary  $U_0$  from  $10^{-4}$  to 100 in one dex intervals. Figure 9 compares the calculation of the models with the observed values. For each  $U_0$  we note on top the appropriate  $\Xi_0$  for the dusty model with  $r = 20$  pc. Other models have  $\Xi_0$  which are offset from the noted value by  $< 0.4$  dex. Models with  $U_0 \gg 0.03$  ( $\Xi_0 \gg 1$ ) are RPC, and their emission line ratios are independent of  $U_0$ , as expected from Figs. 3 and 4. Models with  $U_0 \ll 0.03$  have  $P_{\text{rad}} \ll P_{\text{gas}}$ , and therefore require an additional confinement mechanism which is stronger than RPC. The uncertainty in the expected ratios due to a possible factor of two in  $Z$  or a change of  $\pm 0.2$  in  $\alpha_{\text{ion}}$  is 0.5 dex for [O III]/[O I] and 0.2 dex for the three other ratios.

In the [Ne v]/[O III] panel, the calculations of all RPC models except the dusty  $r = 2$  pc model are within the observed range of values. Therefore, given the uncertainties mentioned above, the observed [Ne v]/[O III] are consistent with a dust-less RPC model with any distribution in  $r$ , and also with a dusty RPC model, as long as the emission of these two lines is not dominated by gas at  $2 L_{1.45}^{1/2}$  pc.

Note that [O III] is efficiently emitted from gas with  $U_0$  as low as  $\approx 10^{-3.5}$ , so in principle gas with  $U_0 \ll 0.03$  can contribute significantly to the observed [O III]. However, the fact that  $U_0 \ll 0.03$  models underpredict the observed [Ne v]/[O III] by orders of magnitude, suggest that it is unlikely that such gas dominate the [O III] emission.

In the [Ne VI]/[Ne III] panel, the dust-less RPC models with  $r = 200$  pc and  $r = 2$  kpc are within the observed range of ratios, while the  $r = 20$  pc and  $r = 2$  pc models are above the mean observed value by a factor of three and five, respectively. Note however that for a broad distribution in  $r$ , a slab at  $r = 2$  pc will not affect the observed [Ne VI]/[Ne III] significantly because both lines are collisionally de-excited (Fig. 6). All dusty RPC models are above the mean observed value by a factor of 3.5. Therefore, the observed [Ne VI]/[Ne III] suggest either a dust-less RPC model, or a dusty RPC model with additional contribution to [Ne III] from  $U_0 \ll 0.03$  slabs, which decreases the observed [Ne v]/[Ne III] ratios from the pure-RPC value. However, given the uncertainty mentioned above, the pure-RPC dusty models cannot be ruled out. A similar behavior is observed in the [Ne v]/[Ne III] panel, where dust-less RPC models are consistent with the observed values, while dusty RPC models with  $r = 20$  pc – 2 kpc overpredict the observed mean value by a factor of 1.5 – 5.

In the [O III]/[O I] panel, the dusty RPC models span the entire range of observed values, and therefore the observed [O III]/[O I] are consistent with a dusty RPC model with slabs from a broad distribution in  $r$ . The RPC dust-less models with  $r \geq 20$  pc overpredict [O III]/[O I] by a factor of 30 – 100. This large difference between the dusty and dust-less models is because the [O III] emissivity decreases due to absorption of ionizing photons by the dust, while the [O I] emission increases because of the photoelectric heating of the gas by the grains. In the  $r = 2$  pc dust-less model,

the calculated [O I] emission per unit  $\Omega$  is enhanced by a factor of 50 compared to models with larger  $r$ . It is not clear whether this huge increase in [O I] emission is a physical effect, or some artifact of the calculation. Therefore, this panel suggests that the gas is dusty, somewhat in contrast with the conclusion from the other panels. In §4, we present additional evidence that the [O III] and [O I] emitting layers are likely dusty, while in the layers which emit [Ne V] and [Ne VI] the dust is at least partially destroyed.

To summarize, the RPC calculations are consistent to within a factor of a few with the observations of unresolved emission line ratios, despite the small dynamical range of emission line ratios permitted by the RPC models.

### 3.3.2 Resolved observations – [Ne III]/[Ne V]

Mazzalay et al. (2010) compared [Ne III]  $\lambda$ 3426/[Ne V]  $\lambda$ 3869 with  $r$  in nine local Seyferts (their fig. 20). Fig. 6 implies that in all the off-center observations of Mazzalay et al., which are at  $r > 10$  pc, the value of [Ne III]/[Ne V] is not expected to change with  $r$  by more than a factor of two<sup>5</sup>. Indeed, Mrk 573, NGC 4507, Mrk 348, NGC 7682, NGC 5643 and NGC 3081 show that [Ne V]/[Ne III] vs.  $r$  is constant up to a factor of about two. In contrast, in non-RPC models, [Ne III]/[Ne V] drops by a factor of 1000 between  $U_0 = 0.1$  and  $U_0 = 10^{-3}$ , similar to the drop in the [Ne V] 14.32  $\mu$ m/[Ne III] 15.55  $\mu$ m ratio seen in the top right panel of Fig. 9. Therefore, non-RPC models will have difficulty explaining why  $U_0$  is so constant at different  $r$ .

The observed values of [Ne III]/[Ne V] in these six objects is in the range 0.4 – 3, compared to [Ne III]/[Ne V] = 0.4 – 0.8 expected in dusty RPC models with  $1 < Z/Z_\odot < 4$  and  $-1.6 < \alpha_{\text{ion}} < -1.2$ , and [Ne III]/[Ne V] = 0.5 – 3 expected in dust-less RPC models with the same range in  $Z$  and  $\alpha_{\text{ion}}$ . Therefore, both the lack of trend of [Ne III]/[Ne V] with  $r$ , and the observed values of [Ne III]/[Ne V], suggest that the gas which emits [Ne III] and [Ne V] in these six objects is RPC. In the other objects, however, some of the observed ratios, at some specific positions, can deviate significantly from RPC, which may indicate non-RPC conditions.

In the six objects with constant [Ne V]/[Ne III] vs.  $r$ , one finds [O II]/[O III] = 0.06 – 0.4. For comparison, dusty RPC models with the range of parameters noted above give [O II]/[O III] = 0.08 – 0.25 in the low  $n_f$  limit. Reddening along the line of sight can decrease [O II]/[O III], while star formation will increase [O II]/[O III]. While the observed [O II]/[O III] are comparable to the expected values at the low  $n_f$  limit, the dispersion per object is larger than expected from a pure-RPC model, and the expected decrease in [O II]/[O III] with decreasing  $r$  is not seen. The fact that [O II]/[O III] does not decrease apparently contradicts RPC. Possibly, projection effects (see §3.1) increase the apparent [O II]/[O III] to the low- $n$  value. This conjecture can be tested using the [O II] line width. If the projected  $r$  is  $< r_{\text{inf}}$ , but the [O II] emission comes from larger  $r$ , then [O II] should not show the expected increase in line width.

### 3.3.3 Resolved observations – $L_{[\text{O III}]}/L_X$

Bianchi et al. (2006) showed that the *Chandra* maps of extended  $L_X$  overlap the *HST* maps of  $L_{[\text{O III}]}$  in eight Seyfert 2s, selected from the FIR-bright Schmitt et al. (2003) catalog based on the

availability of a *Chandra* observation. Spectroscopy showed that  $L_X$  is dominated by emission lines, which likely arise in photoionized gas. Bianchi et al. used this overlap to show that  $U$  is independent of  $r$ , and therefore  $n \propto r^{-2}$ . As can be seen in Fig. 6, this nearly constant  $L_{[\text{O III}]}/L_X$  is a direct consequence of RPC, under the condition that  $n_f \ll n_{\text{crit}}([\text{O III}])$ , which is satisfied for the Bianchi et al. observations<sup>6</sup>. In other words, RPC gives a physical interpretation for the  $n \propto r^{-2}$  relation found by Bianchi et al.

The observed  $L_{[\text{O III}]}/L_X$  in the Bianchi et al. (2006) objects are 2.8 – 4.8, except NGC 7212 which has  $L_{[\text{O III}]}/L_X = 11$ . In the low- $n$  limit, the dusty  $Z = 2Z_\odot$  RPC models give  $L_{[\text{O III}]}/L_X = 1.4, 5.7, \text{ and } 23$  for  $\alpha_{\text{ion}} = -1.2, -1.4, \text{ and } -1.6$ , respectively. Increasing or decreasing  $Z$  by a factor of two changes  $L_{[\text{O III}]}/L_X$  by  $< 40\%$ . Therefore, the observed  $L_{[\text{O III}]}/L_X$  are in the range of  $L_{[\text{O III}]}/L_X$  derived from the RPC models using reasonable values of  $\alpha_{\text{ion}}$ .

## 3.4 Emission line ratios: BPT

G04 calculated the BPT ratios (Baldwin, Phillips & Terlevich 1981; Veilleux & Osterbrock 1987) of dusty models with  $n_f = 10^2 - 10^4 \text{ cm}^{-3}$ . The G04 models include both RPC models with  $U_0 \gg 0.03$ , and models with  $U_0 \ll 0.03$  which are effectively constant- $n$  models. Kewley et al. (2006, hereafter K06) compared the G04 models with SDSS Seyferts in the [O III]/H $\beta$  vs. [O I]/H $\alpha$  BPT diagram (fig. 23 there). The shown range of emission line ratios implied by the different  $U_0$  is basically of non-RPC models, since the RPC models all converge to a single solution, as noted in G04. K06 found that the BPT ratios of RPC slabs are consistent with the high-[O III]/H $\beta$  end of the observed distribution in SDSS Seyferts.

Here, we extend the K06 analysis to a distribution of slabs with  $10^{-1.5} \leq n_f \leq 10^{7.5} \text{ cm}^{-3}$ , implying  $1 < n_f < 10^9 \text{ cm}^{-3}$ . We use only RPC models ( $U_0 \gg 0.03$ ), where the emission line ratios are independent of  $U_0$ . Slabs with  $n_f < 1 \text{ cm}^{-3}$  are disregarded since the ambient ISM pressure will likely dominate the radiation pressure (Fig. 1), and such slabs will not be RPC. This minimum  $n_f$  corresponds to  $r_{\text{out}} = 1.2 L_{1,43}^{1/2} \text{ kpc}$  (eq. 20). Slabs with  $n_f \geq 10^{8.5} \text{ cm}^{-3}$  are disregarded because they are part of the BLR<sup>7</sup>. We assume a power law distribution with index  $\eta$  (eq. 24), and sum the emission from different slabs weighted by the implied  $d\Omega$ .

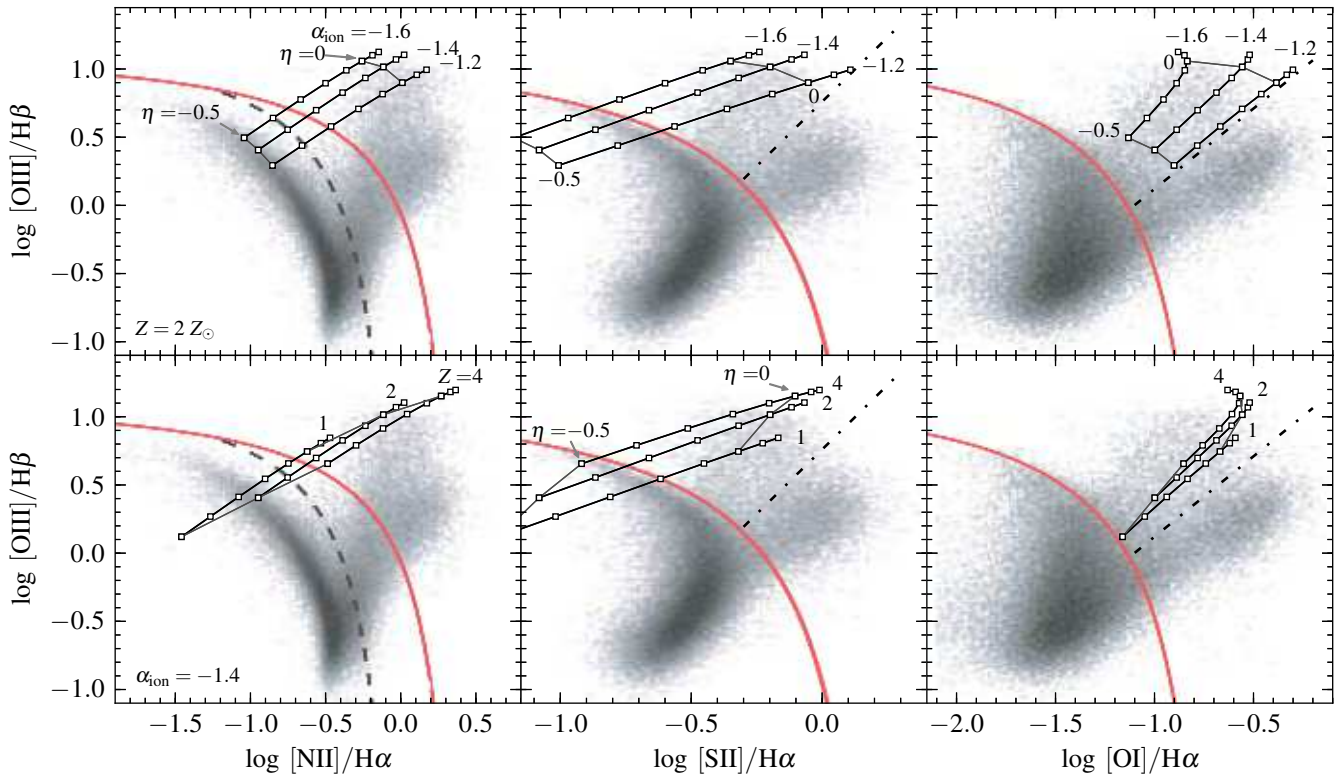
Note that in type 2 AGN the high  $n_f$  gas near the center may be obscured, and therefore should not enter the calculation, though at which  $n_f$  this occurs is not well-constrained. In the BPT ratios, decreasing  $\eta$  and lowering the maximum  $n_f$  is degenerate, so the  $\eta$  derived below may be somewhat overestimated. However, the similarity of the BPT ratios in type 1 and type 2 AGN which are selected similarly (Stern & Laor 2013) implies that obscuration does not play a significant role in the BPT ratios.

Figure 10 compares the RPC calculations with the emission line measurements of SDSS galaxies (fig. 1 in K06). We add several commonly used classification lines: the theoretical classification lines from Kewley et al. (2001) which separate star forming (SF) galaxies and AGN (red solid lines), the empirical classification line from Kauffmann et al. (2003), which separate pure-SF and

<sup>5</sup> None of the Mazzalay et al. (2010) objects is likely to have  $L_{\text{ion}} > 10^{46} \text{ erg s}^{-1}$ .

<sup>6</sup> Fig. 6 shows that  $n_f = n_{\text{crit}}([\text{O III}]) = 10^{5.8} \text{ cm}^{-3}$  at  $r = 16 L_{1,45}^{1/2} \text{ pc}$ , while the extended emission in the Bianchi et al. (2006) maps is on scales  $\gg 25 \text{ pc}$ . None of the Bianchi et al. (2006) objects is likely to have  $L_{\text{bol}} \gg 10^{45.5} \text{ erg s}^{-1}$ .

<sup>7</sup> As mentioned above, our models do not include the expected sublimation of small grains at  $n_f > 10^{5.9} \text{ cm}^{-3}$ .



**Figure 10.** Expected BPT ratios for an ensemble of RPC slabs with a distribution in  $r$ , compared to observations of SDSS galaxies. Each black line marks the RPC calculations, for  $Z = 2Z_{\odot}$  and different  $\alpha_{\text{ion}}$  (top panels,  $\alpha_{\text{ion}}$  noted), or for  $\alpha_{\text{ion}} = -1.4$  and different  $Z$  (bottom panels,  $Z$  noted). The white squares mark different  $\eta$ , where  $\eta$  is the index of the slab covering factor distribution as a function of  $r$  (eq. 24). The  $\eta$  vary between  $-0.5$  and  $0.2$  in steps of  $0.1$ . Same- $\eta$  models with  $\eta = 0$  or  $\eta = -0.5$  are connected by a thin gray line, and  $\eta$  is noted. Lower  $\eta$  produce lower ratios of forbidden lines to recombination lines, due to the collisional de-excitation of the forbidden lines at small  $r$ . The background shows the observed emission line ratios in SDSS emission line galaxies (fig. 1 in K06), and the various classification lines from Kewley et al. (2001), Kauffmann et al. (2003), and K06. Seyferts reside above the solid red and black dash-dotted lines. The RPC model with  $\alpha_{\text{ion}} \lesssim -1.4$ ,  $Z \gtrsim 2Z_{\odot}$  and  $\eta \sim -0.1$  reproduces the observed BPT ratios at the high-[O III]/H $\beta$  end of the Seyfert distribution. All of these parameters are expected from independent observations. An additional star forming component is required to explain the entire distribution of BPT ratios in SDSS Seyferts.

SF-AGN ‘Composites’ (dashed line in the [N II]/H $\alpha$  panel), and the K06 empirical separation between Seyferts and LINERs (dash-dotted lines in the [S II]/H $\alpha$  and [O I]/H $\alpha$  panels). Each black solid line represents the RPC calculation for  $-0.5 \leq \eta \leq 0.2$ , with white squares representing steps of  $0.1$  in  $\eta$ . The top panels show models with  $Z = 2Z_{\odot}$  and several reasonable values of  $\alpha_{\text{ion}}$ , while the bottom panels show models with  $\alpha_{\text{ion}} = -1.4$  and several reasonable values of  $Z$ . Lower  $\eta$  produce lower BPT ratios, due to collisional de-excitation of the forbidden lines in slabs with small  $r$ , which are more significant at low  $\eta$ .

RPC models with  $Z = 2Z_{\odot}$ ,  $\alpha_{\text{ion}} = -1.4$ , and  $\eta \approx -0.1$  reproduce the observed BPT ratios at the high-[O III]/H $\beta$  end of the Seyfert distribution. Models with  $\eta \approx -0.1$  and  $Z = 4Z_{\odot}$  or  $\alpha_{\text{ion}} = -1.2$  are also generally within the observed range of values, though they overpredict the observed [O I]/H $\alpha$  in most Seyferts by  $\sim 0.2$  dex. The  $\eta \approx -0.1$  implied by the BPT diagrams is consistent with the  $\eta \sim 0$  expected from the flat IR slope in the mean quasar SED (§2.7). Therefore, the conclusion of K06 mentioned above applies also when summing slabs with a broad distribution of  $n$ . As noted by K06, an additional SF component is required to reproduce the entire observed distribution of BPT ratios in SDSS Seyferts.

### 3.5 The extent of RPC in type 2 quasars

Recently, Liu et al. (2013a) resolved [O III]/H $\beta$  in  $z \sim 0.5$  type 2 quasars selected from the Zakamska et al. (2003) sample, with a resolution of  $\sim 3$  kpc. They find a constant [O III]/H $\beta = 12.3 \pm 2.7$  extending out to  $r = r_{\text{break}}$ , with  $4 < r_{\text{break}} < 11$  kpc. At  $r > r_{\text{break}}$ , [O III]/H $\beta$  declines with  $r$ . In RPC, a constant [O III]/H $\beta = 13$  is expected at  $r > 300 L_{1,45}^{1/2}$  pc (Fig. 6), consistent with the observed [O III]/H $\beta$  at  $r < r_{\text{break}}$  and the  $L_{\text{ion}} = 10^{46} - 10^{47}$  erg s $^{-1}$  of the Liu et al. sample<sup>8</sup>.

The decrease in [O III]/H $\beta$  at  $r > r_{\text{break}}$  may indicate that the ambient pressure  $P_{\text{gas},0}$  exceeds  $P_{\text{rad}}$ , causing  $U_0$  to decrease with increasing  $r$ . Therefore,  $r_{\text{break}}$  is the maximum  $r$  where RPC is applicable. Since the value of  $r$  where  $P_{\text{gas},0} = P_{\text{rad}}$  depends on  $L_{\text{bol}}$  and on  $P_{\text{gas},0}$ , we expect a correlation between  $r_{\text{break}}$  and  $L_{\text{bol}}$ . Indeed,  $r_{\text{break}}$  and  $L_{[\text{O III}]}$  have a Pearson correlation coefficient of  $0.45$  in the Liu et al. sample, with a 12% chance of random occurrence. Hence, there is a possible relation between  $L_{[\text{O III}]}$  and  $r_{\text{break}}$ , as expected from RPC, though more data is required for a defini-

<sup>8</sup> We derived  $L_{\text{ion}}$  from the  $L_{[\text{O III}]}$  listed in Liu et al. (2013b) and the  $L_{\text{bol}}$  vs.  $L_{[\text{O III}]}$  relation of Stern & Laor (2012b).



tive answer. The implied  $P_{\text{gas},0}(r_{\text{break}})$  is  $220 \pm 98 \text{ cm}^{-3}$  (in units of  $2.3 \cdot 10^4 K_{\text{B}}$ ).

## 4 DUST EXISTENCE

In Fig. 4 we showed that dust has a significant effect on the RPC slab structure. In this section, we present the relevant theoretical considerations and observational evidence for the existence of dust in ionized gas in AGN.

### 4.1 Theoretical considerations

#### 4.1.1 Grain sublimation

Fig. 8 in [Laor & Draine \(1993\)](#) shows the values of  $rL_{\text{bol}}^{-1/2}$  where grains with different compositions and sizes sublimate. Assuming  $\langle h\nu \rangle = 36 \text{ eV}$  and  $L_{\text{ion}} = 0.35L_{\text{bol}}$ , as above, Silicate grains with radii  $a = 0.005, 0.25$  and  $10 \mu\text{m}$  sublimate at  $n_{\gamma} = 10^{5.9}, 10^{7.3}$  and  $10^{8.3} \text{ cm}^{-3}$ , respectively. Graphite grains with the same  $a$  sublimate at  $n_{\gamma} = 10^7, 10^{8.6}$  and  $10^{8.6} \text{ cm}^{-3}$ . Therefore, at  $n_{\gamma} > 10^{8.6} \text{ cm}^{-3}$  all dust grains sublimate. At  $10^{5.9} < n_{\gamma} < 10^{8.6} \text{ cm}^{-3}$ , the dust content strongly depends on  $n_{\gamma}$ .

#### 4.1.2 Grain sputtering

Another source of grain destruction is sputtering due to collisions with gas particles. The sputtering efficiency depends on the relative velocity between the grain and individual gas particles. This velocity is either the sound speed  $c_s$ , or the dust drift velocity in the gas rest frame  $v_{\text{drift}}$ , if the drift is supersonic. For stationary grains sputtering is efficient at  $T > 10^5 - 10^6 \text{ K}$ , or  $c_s > 40 - 130 \text{ km s}^{-1}$  ([Draine 2011b](#)). Most line emission in the RPC slab occurs at lower  $T \ll 10^5 \text{ K}$  (see appendix A), so without  $v_{\text{drift}} \gg c_s$ , sputtering is unlikely to have a significant effect on the dust content in the line-emitting layer of the slab. Accurate calculation of  $v_{\text{drift}}$  in AGN has not been performed yet, and is beyond the scope of this work. However, it is relatively straightforward to derive an upper limit on  $v_{\text{drift}}$ , so it is possible to understand in which layers sputtering is possible, and in which layers it is unlikely.

The terminal  $v_{\text{drift}}$  of a neutral grain can be derived by balancing the radiation force on the grain with the force of collisional drag (e.g. [Draine & Salpeter 1979](#)). In the limit of highly supersonic drift,

$$\frac{L_{\text{bol}}}{4\pi r^2 c} \langle Q_{\text{pr}} \rangle \pi a^2 = \pi a^2 n m_{\text{p}} v_{\text{drift}}^2 \quad (30)$$

where  $\langle Q_{\text{pr}} \rangle \pi a^2$  is the radiation pressure cross section averaged over the incident spectrum ([Draine 2011b](#)). Replacing  $L_{\text{bol}}/(4\pi r^2 c)$  with  $1.5\beta P_{\text{rad}}$ , appropriate for the  $\beta = 1.9$  derived above and the  $L_{\text{ion}} = 0.35 L_{\text{bol}}$  in our assumed SED, we get

$$1.5 \langle Q_{\text{pr}} \rangle \beta P_{\text{rad}} = n m_{\text{p}} v_{\text{drift}}^2 = n m_{\text{p}} v_{\text{drift}}^2 \left( \frac{2KT}{m_{\text{p}} c_s^2} \right) = P_{\text{gas}} \left( \frac{v_{\text{drift}}}{c_s} \right)^2 \\ \Rightarrow \left( \frac{v_{\text{drift}}}{c_s} \right)^2 = 1.5 \langle Q_{\text{pr}} \rangle \frac{\beta P_{\text{rad}}}{P_{\text{gas}}} = 1.5 \langle Q_{\text{pr}} \rangle \Xi = 1.5 \langle Q_{\text{pr}} \rangle \tau^{-1} \quad (31)$$

where we used eq. 11 in the last equality, which is valid at  $\tau < 1$ . Charged grains will also experience Coulomb drag, which may decrease  $v_{\text{drift}}$ .

The value of  $\langle Q_{\text{pr}} \rangle$  is unlikely to be larger than  $\sim 2$  (e.g. [Laor & Draine 1993](#)). Therefore, at  $\tau = 0.3$ , where  $T = 30,000 \text{ K}$

(Fig. 2), we find  $v_{\text{drift}} \leq (1.5 \cdot 2 \cdot \tau^{-1})^{1/2} c_s = 70 \text{ km s}^{-1}$ , and sputtering may be efficient in destroying the grains. The dependence of  $v_{\text{drift}}/c_s$  on  $\langle Q_{\text{pr}} \rangle$ , together with the dependence of the sputtering efficiency at a certain  $T$  on grain properties, can lead to a situation where only part of the dust is destroyed in this layer. Near the ionization front, where  $\Xi \approx 1$  and  $T \approx 10^4 \text{ K}$ , sputtering is highly ineffective.

### 4.2 Observational constraints

As noted above, dust survival depends on the depth within the slab. We therefore divide the slab into two different layers, and analyze the observational evidence for dust existence in each of them.

#### 4.2.1 Inner layer (IP $\lesssim 40 \text{ eV}$ )

The layer which emits [O III] and other lines with similar or lower IP occurs at  $\tau \gtrsim 1.5$  (app. A), where dust grains will likely survive. There are several indications that this inner layer of the NLR is indeed dusty. First, [Galliano et al. \(2003, 2005\)](#) found that the extended MIR emission in NGC 1068 is well correlated with the [O III] emission, suggesting that presence of dust grains in the line-emitting gas. Second, the observed [O III]/[O I] (lower left panel in Fig. 9) suggest a dusty RPC model. A third piece of evidence is the lack of detection of [Ca II] 7291Å in AGN, which suggests that Ca is highly depleted onto dust grains ([Ferland 1993](#); [Villar-Martin & Binette 1997](#); [Ferguson et al. 1997](#); [Shields et al. 1999](#); [Cooke et al. 2000](#)). The dust-less RPC model with  $Z = 2Z_{\odot}$ ,  $\alpha_{\text{ion}} = -1.6$  and  $\eta = 0$  gives [Ca II]/[S II]  $\lambda 6716 = 0.11$ . For comparison, the mean SDSS spectrum from [Vanden Berk et al. \(2001\)](#) shows a prominent [S II] feature, while [Ca II] is not detected, suggesting [Ca II]/[S II]  $< 0.02$ . Therefore, Ca is depleted by at least a factor of  $\sim 5$ , implying the existence of dust in this low IP layer.

#### 4.2.2 Outer layer (IP $\gtrsim 100 \text{ eV}$ )

Ne<sup>4+</sup> (IP = 97 eV) appears at  $\tau \sim 0.3 - 1.5$  (app. A). At the low  $\tau$  end of this layer, sputtering may be efficient in destroying the grains (see above). The [Fe VII]  $\lambda 6087$ /[Ne V]  $\lambda 3426$  ratio has been suggested as a good tracer of the relative abundance of these two elements, due to the similar IP of the two ions ([Nussbaumer & Osterbrock 1970](#)). Therefore, the ratio of these two lines is a good measure of Fe depletion, which is depleted by a factor of 100 in the dusty ISM. [Vanden Berk et al. \(2001\)](#) and [Shields et al. \(2010\)](#) found a mean [Fe VII]/[Ne V] = 0.3 in SDSS quasars, while [Nagao et al. \(2003\)](#) found [Fe VII] / [Ne V] =  $0.5 \pm 0.3$  in nearby type 1 AGN and  $0.3 \pm 0.2$  in nearby type 2 AGN. For comparison, the RPC dusty model with  $Z = 2Z_{\odot}$ ,  $\alpha_{\text{ion}} = -1.6$  and  $\eta = 0$  gives [Fe VII] / [Ne V] = 0.012. while the dust-less model with the same parameters gives [Fe VII] / [Ne V] = 0.55. Therefore, the abundance of Fe, relative to the abundance of Ne, is much higher than the depleted abundance seen in the ISM. A similar conclusion was reached by [Ferguson et al. \(1997\)](#), D02, [Nagao et al. \(2003\)](#) and [Shields et al. \(2010\)](#).

The high abundance of Fe relative to the depleted abundance implies that if grains existed in this layer at some period, a non-negligible fraction of them has been destroyed. However, we note that even if 50% of the dust has been destroyed, the Fe abundance would increase by a factor of 50, and thus be similar to the abundance in a dust-less model, while  $\bar{\sigma}$  will decrease only by a factor



of two, and thus the slab structure would be similar to the dusty models. For the dust opacity to decrease to  $\sigma_{\text{Th}}$ , 99.9% of the dust needs to be destroyed (see eqs. 18–19). A selective destruction of grains is likely under some conditions due to the dependence of the destruction mechanisms on grain properties (see previous section). Therefore, abundance measures are not robust ways to determine whether the dust opacity has been significantly reduced, and the question of whether some dust exists in this outer layer remains open.

## 5 DISCUSSION AND IMPLICATIONS

### 5.1 Validity of the RPC assumptions

The RPC structure is calculated using the radiative force exerted by the ionizing radiation. When does the radiative force dominate? We define the radiative force per H-nucleus, normalized by  $m_p$ , as  $f_{\text{rad}}$ . At the illuminated surface of a dusty slab,

$$f_{\text{rad}} = \frac{\beta P_{\text{rad}} \bar{\sigma}}{m_p} = 1.4 \times 10^{-4} L_{i,45} r_{50}^{-2} \bar{\sigma}_{-21} \text{ cm s}^{-2} \quad (32)$$

The gas may reside in a typical giant molecular cloud (GMC). In this case the self-gravity force  $f_{\text{GMC}}$  is

$$f_{\text{GMC}} = 1.5 \times 10^{-8} \frac{M_{\text{GMC}}}{10^5 M_{\odot}} \left( \frac{d_{\text{GMC}}}{10 \text{ pc}} \right)^{-2} \text{ cm s}^{-2} \quad (33)$$

where  $M_{\text{GMC}}$  and  $d_{\text{GMC}}$  are the the mass and size of the cloud, respectively.

Another force which may be significant in the ISM is radiation pressure from stellar light  $f_{\text{star}}$ . Adopting  $P_{\text{rad}} = u/3$ , for an isotropic radiation field, where  $u = 8.6 \times 10^{-13} \text{ erg s}^{-1} \text{ cm}^{-3}$  (Draine 2011b) is the energy density of the stellar radiation in the Galaxy, gives

$$f_{\text{star}} = 1.8 \times 10^{-11} \text{ cm s}^{-2} \quad (34)$$

where we used  $\bar{\sigma} = 10^{-22} \text{ cm}^2$  which is the dust absorption cross section at the peak of the stellar emission, around  $1 \mu\text{m}$ . Clearly, the AGN radiative force dominates the force from the ambient stellar light, on all scales, as expected if the AGN is more luminous than the host galaxy.

For a GMC, we get that  $f_{\text{rad}} > f_{\text{GMC}}$  at  $r < 4.8 L_{i,45}^{1/2} \text{ kpc}$ . Thus, once the AGN luminosity clearly dominates the host luminosity, i.e.  $L_{\text{bol}} > 10^{44} \text{ erg s}^{-1}$ , the AGN radiative force can dominate the self-gravity of a GMC quite far out on the host galaxy scale. This force can compress the GMC, and possibly affect the star formation rate on large scales in the host galaxy.

We note in passing that photoionized gas may be confined even when it is optically thin and radiatively accelerated. In the accelerated frame there will still be a differential acceleration, a factor of  $\tau$  smaller than for a static slab, which will lead to a correspondingly smaller pressure gradient, and therefore densities also a factor of  $\tau$  smaller. The structure of such a layer has been explored in various studies on AGN (Weymann 1976; Scoville & Norman 1995; Chelouche & Netzer 2001), and may be subject to various instabilities (Mathews & Blumenthal 1977; Mathews 1982, 1986).

### 5.2 Comparison with LOC

The locally optimal emitting clouds model (LOC, Ferguson et al. 1997) suggests that the narrow line emission in AGN originates from an ensemble of clouds with a distribution of  $U$  and  $n$ , where

each line originates from the LOC which maximizes its emission. For comparison, the RPC solution can be viewed as a superposition of uniform density optically thin slabs situated one behind the other, with  $U$  going down from  $\sim 100$  to  $\sim 1$ , and an optically thick slab with  $U \lesssim 0.1$  on the back side. Therefore, RPC implies that there is a range of  $U$  at a given distance, as suggested by LOC, but in RPC the distribution in  $U$  can be calculated, rather than being a free parameter. Similarly,  $n$  is set by  $L_{\text{ion}}$  and  $r$  in RPC, rather than being a free parameter.

### 5.3 LINERS

The background of Fig. 10, taken from K06, shows the spread of BPT ratios in SDSS galaxies where the emission lines are excited by a hard spectrum (above the red lines). K06 showed that these BPT ratios have a bi-modal distribution, indicating the existence of two distinct groups, known as Seyferts and LINERS. K06 used G04 models with  $U_0 < 0.03$ , which are effectively constant- $n$  models, to show that the different narrow line ratios imply a different  $U$ , where  $U \sim 10^{-3}$  in LINERS, compared to  $U \sim 10^{-2} - 10^{-2.5}$  in Seyferts, confirming earlier results by Ferland & Netzer (1983). Moreover, LINERS have been found to be distinct from Seyferts also in  $\dot{m}$  (K06; fig. 9 in Antonucci 2012; Stern & Laor 2013), where Antonucci and Stern & Laor found a transition  $\dot{m}$  of  $10^{-3}$ .

Since a transition in the accretion flow is theoretically expected at low  $\dot{m}$  (Abramowicz et al. 1995; Narayan & Yi 1995), the different  $U$  are thought to be a result of the different incident SED (K06; Ho 2008). However, why a lower  $U$  follows from a different incident SED has not been explained. RPC may provide the missing link between  $U$  and  $\beta \langle hv \rangle$ , quantitatively. Eq. 7 shows that a factor of 3–10 difference in  $U_f$  implies a factor of 3–10 difference in  $\beta \langle hv \rangle$ . Hence, if LINERS are RPC, then either the ionizing spectrum is harder in LINERS (larger  $\langle hv \rangle$ ), or the ratio of optical to ionizing photons is higher (larger  $\beta$ ), or both. The exact difference in  $\beta \langle hv \rangle$  requires RPC modeling of LINERS with their observed SED.

### 5.4 $M_{\text{BH}}$ estimates

The coefficient of the  $v \propto n_{\text{crit}}^{1/4}$  relation (eq. 28) depends on  $M_{\text{BH}}$ . Therefore, this relation can be used to estimate  $M_{\text{BH}}$  using the  $v$  and  $n_{\text{crit}}$  of the forbidden emission lines. From eq. 28 we get

$$M_{\text{BH}} = 2 \times 10^7 v_{300}^2 (\beta L_{i,43})^{1/2} n_{\text{crit},6}^{-1/2} M_{\odot} \quad (35)$$

where  $v = 300 v_{300} \text{ km s}^{-1}$ , and we explicitly noted the dependence on  $\beta$ , which may be higher in LINERS than in Seyferts (see previous section). Eq. 35 can be used to estimate  $M_{\text{BH}}$  from each forbidden line which is emitted from  $r \ll r_{\text{inf}}$ , i.e. all lines with  $n_{\text{crit},6} \gg 160 \dot{m}$  (eq. 27). Therefore, this method for estimating  $M_{\text{BH}}$  is most effective in AGN with low  $\dot{m}$ , where a larger fraction of the narrow line region enters the sphere of influence of the black hole.

For each object in Fig. 8, we find the  $M_{\text{BH}}$  which best-fits the observed  $v$  vs.  $n_{\text{crit}}$ , for all lines with  $n_{\text{crit},6} > 160 \dot{m}$ . Note that the lines which enter the fit depend on  $M_{\text{BH}}$ . We use the values of  $L_{\text{ion}}$  listed in Table 1 and  $\beta = 2$ . These estimates of  $M_{\text{BH}}$  are listed in Table 1.

In low  $\dot{m}$  AGN the host is clearly detectable by selection. One can therefore explore the relation of the directly measured  $M_{\text{BH}}$ , based on gas dynamics within the black hole sphere of influence,

with various host properties, such as the bulge mass, velocity dispersion, etc’.

### 5.5 The covering factor

In dust-less gas with NLR densities, the emitted  $H\alpha$  flux is determined by the flux of incident ionizing photons. Therefore,  $L_{\text{line}}(H\alpha)/L_{\text{ion}}$  is a measure of  $\Omega$ . In dusty gas, one needs to correct for the absorption of ionizing photons by dust grains. For a typical dust distribution and AGN SED, dust dominates the opacity of ionizing photons at  $U > 0.006$  (Netzer & Laor 1993). In RPC most of the absorption occurs at  $U > U_f = 0.03$  (eq. 7), so the fraction of ionizing photons which ionize the gas  $f_{\text{ion}}$  is expected to be  $\ll 1$ . Indeed, in the RPC models with  $\eta = 0$  and  $\alpha_{\text{ion}} = -1.6$  we find  $f_{\text{ion}} = 1/7, 1/9,$  and  $1/12$  for  $Z/Z_{\odot} = 1, 2$  and  $4$ , respectively. Values of  $\alpha_{\text{ion}}$  between  $-1.2$  and  $-1.8$  change  $f_{\text{ion}}$  by  $\pm 20\%$ .

Stern & Laor (2012b) showed that if the absorption of ionizing photons by grains is neglected,  $\Omega(f_{\text{ion}} = 1) = 0.04$  at  $L_{\text{bol}} = 10^{45.5} \text{ erg s}^{-1}$ . For a typical  $Z = 2Z_{\odot}$ , this value of  $\Omega(f_{\text{ion}} = 1)$  implies  $\Omega = 9\Omega(f_{\text{ion}} = 1) = 0.36$ . However, Stern & Laor also found that  $\Omega(f_{\text{ion}} = 1) \propto L_{\text{bol}}^{-0.3}$ , reaching  $\Omega(f_{\text{ion}} = 1) = 0.4$  at  $L_{\text{bol}} = 10^{42.5} \text{ erg s}^{-1}$ . Using the  $f_{\text{ion}}$  derived above we will find an unphysical  $\Omega > 1$  at low  $L_{\text{bol}}$ . Hence, either  $f_{\text{ion}}$  is underestimated at all  $L_{\text{bol}}$ , or  $f_{\text{ion}}$  increases with decreasing  $L_{\text{bol}}$ .

The true  $f_{\text{ion}}$  might be somewhat higher than we derived due to the dust destruction mechanisms described in §4, which we do not model. Also,  $f_{\text{ion}}$  may increase with decreasing  $L_{\text{bol}}$ , due to two reasons. First, lower  $L_{\text{bol}}$  AGN likely reside in host galaxies with lower  $M_*$  and therefore lower  $Z$ , which implies a higher  $f_{\text{ion}}$ . Second, an increase of  $\beta\langle hv \rangle$  with decreasing  $L_{\text{bol}}$  will cause  $U_f$  to decrease (see §5.3) and hence increase  $f_{\text{ion}}$ .

## 6 CONCLUSIONS

Radiation Pressure Confinement is inevitable for a hydrostatic solution of ionized gas, since the transfer of energy from the radiation to the gas is always associated with momentum transfer. Only confinement mechanisms which are stronger than RPC, or non-hydrostatic conditions, can obviate RPC. The success of RPC in reproducing the observations (§3) suggests that these alternatives are not dominant in AGN.

We expand on the earlier study of D02 and G04 of the RPC solution for the NLR, and study the global structure of the photoionized gas on scales outside the BLR. RPC implies the following:

- (i) The value of  $n$  is determined by  $L_{\text{ion}}$  and  $r$ , via eq. 6. This relation is observed in resolved observations of the NLR, in the FWHM vs.  $n_{\text{crit}}$  relation first observed by Filippenko & Halpern (1984), and in the comparison of  $n_{\text{BLR}}$  with  $r_{\text{BLR}}$  (Paper II). Together, these observations span a dynamical range of  $\sim 10^4$  in  $r$ , from sub-pc scale to kpc scale, and a range of  $\sim 10^8$  in  $n$ , from  $10^3$  to  $10^{11} \text{ cm}^{-3}$ .
- (ii) The hydrostatic solution of RPC gas is independent of the boundary value  $U_0, n_0$  or  $P_{\text{gas},0}$ . Therefore, if  $r$  is known, RPC models have essentially zero free parameters.
- (iii) The ionization structure of RPC slabs is unique, including a highly ionized X-ray emitting surface, an intermediate layer which emits coronal lines, and a lower ionization inner layer which emits optical lines. The fraction of radiation energy absorbed in each ionization state is given by eq. 12. This structure can explain the overlap of the extended X-ray and narrow line emission, and some spatially resolved narrow line ratios.

- (iv) Beyond the sublimation radius, the line emitting gas is likely to be dusty, at least in the layers which emit the [O III] and lower ionization lines. The dust thermal IR emission constitutes  $\sim 80\%$  of the total emission, and line emission the remaining  $\sim 20\%$ , at all  $r$ . Therefore, RPC implies that there is no distinction between an IR-emitting torus, and a line-emitting NLR.
- (v) The value of  $U_f$ , which is the typical ionization parameter where most of the radiation is absorbed, is set solely by the SED of the incident spectrum. Therefore LINERs, which have a lower  $U_f$  than Seyferts, are expected to have a higher  $\beta\langle hv \rangle$ .
- (vi) Following G04 and K06, we find that BPT ratios implied by RPC are consistent with observations of SDSS galaxies, assuming a nearly constant covering factor per unit  $\log r$ . This covering factor distribution is expected from the flat IR slope observed in AGN.
- (vii) RPC predicts that  $\text{FWHM} \propto n_{\text{crit}}^{1/4}$  for  $n_{\text{crit}} > 1.6 \times 10^8 \text{ cm}^{-3}$ , and implies that the normalization of the  $\text{FWHM} \propto n_{\text{crit}}^{1/4}$  relation (eq. 28) depends on  $M_{\text{BH}}$ . Therefore,  $M_{\text{BH}}$  can be estimated directly by measuring the gas dynamics. This method is effective in low  $\dot{m}$  AGN, where many forbidden lines are emitted inside the radius of influence of the black hole. In such objects the host is expected to be well resolved, and one can therefore explore the relation between the host properties and the  $M_{\text{BH}}$  derived from the gas dynamics.

## ACKNOWLEDGEMENTS

We thank Jonelle Walsh for providing her *HST* observations of the NLR in nearby AGN. Numerical calculations were performed with version C10.00 of Cloudy, last described by Ferland et al. (1998). This publication makes use of data products from the SDSS project, funded by the Alfred P. Sloan Foundation.

## REFERENCES

- Abazajian, K. N., et al. 2009, *ApJS*, 182, 543  
 Abramowicz, M. A., Chen, X., Kato, S., Lasota, J.-P., & Regev, O. 1995, *ApJ*, 438, L37  
 Antonucci, R. 2012, *Astronomical and Astrophysical Transactions*, 27, 557  
 Appenzeller, I., & Oestreicher, R. 1988, *AJ*, 95, 45  
 Baldwin, J. A., Phillips, M. M., & Terlevich, R. 1981, *PASP*, 93, 5  
 Balmaverde, B., Capetti, A., Grandi, P., et al. 2012, *A&A*, 545, A143  
 Barth, A. J., Ho, L. C., Filippenko, A. V., Rix, H.-W., & Sargent, W. L. W. 2001, *ApJ*, 546, 205  
 Baskin, A., Laor, A., Stern, J. 2013, in preparation (Paper II)  
 Begelman, M., de Kool, M., & Sikora, M. 1991, *ApJ*, 382, 416  
 Bennert, N., Jungwiert, B., Komossa, S., Haas, M., & Chini, R. 2006a, *A&A*, 456, 953  
 Bennert, N., Jungwiert, B., Komossa, S., Haas, M., & Chini, R. 2006b, *A&A*, 459, 55  
 Bianchi, S., Guainazzi, M., & Chiaberge, M. 2006, *A&A*, 448, 499  
 Bower, G. A., Wilson, A. S., Heckman, T. M., et al. 2000, *Bulletin of the American Astronomical Society*, 32, 1566  
 Chelouche, D., & Netzer, H. 2001, *MNRAS*, 326, 916  
 Chevallier, L., Czerny, B., Róańska, A., & Gonçalves, A. C. 2007, *A&A*, 467, 971  
 Collins, N. R., Kraemer, S. B., Crenshaw, D. M., Bruhweiler, F. C., & Meléndez, M. 2009, *ApJ*, 694, 765

- Cooke, A. J., Baldwin, J. A., Ferland, G. J., Netzer, H., & Wilson, A. S. 2000, *ApJS*, 129, 517
- Dadina, M., Guainazzi, M., Cappi, M., et al. 2010, *A&A*, 516, A9
- Davidson, K., & Netzer, H. 1979, *Reviews of Modern Physics*, 51, 715
- Davis, S. W., & Laor, A. 2011, *ApJ*, 728, 98
- de Bruyn, A. G., & Wilson, A. S. 1978, *A&A*, 64, 433
- Devereux, N., Ford, H., Tsvetanov, Z., & Jacoby, G. 2003, *AJ*, 125, 1226
- Dopita, M. A., Groves, B. A., Sutherland, R. S., Binette, L., & Cecil, G. 2002, *ApJ*, 572, 753
- Draine, B. T., & Salpeter, E. E. 1979, *ApJ*, 231, 77
- Draine, B. T. 2011a, *ApJ*, 732, 100
- Draine, B. T. 2011b, *Physics of the Interstellar and Intergalactic Medium* by Bruce T. Draine. Princeton University Press, 2011. ISBN: 978-0-691-12214-4
- Emmering, R. T., Blandford, R. D., & Shlosman, I. 1992, *ApJ*, 385, 460
- Espey, B. R., Turnshek, D. A., Lee, L., et al. 1994, *ApJ*, 434, 484
- Ferguson, J. W., Korista, K. T., Baldwin, J. A., & Ferland, G. J. 1997, *ApJ*, 487, 122
- Ferland, G. J., & Netzer, H. 1983, *ApJ*, 264, 105
- Ferland, G. J., Peterson, B. M., Horne, K., Welsh, W. F., & Nahar, S. N. 1992, *ApJ*, 387, 95
- Ferland, G. J., Korista, K. T., Verner, D. A., Ferguson, J. W., Kingdon, J. B., & Verner, E. M. 1998, *PASP*, 110, 761
- Ferland, G. J. 1993, *The Nearest Active Galaxies*, 75
- Filippenko, A. V., & Halpern, J. P. 1984, *ApJ*, 285, 458
- Filippenko, A. V. 1985, *ApJ*, 289, 475
- Filippenko, A. V., & Sargent, W. L. W. 1988, *ApJ*, 324, 134
- Galliano, E., Alloin, D., Granato, G. L., & Villar-Martín, M. 2003, *A&A*, 412, 615
- Galliano, E., Pantin, E., Alloin, D., & Lagage, P. O. 2005, *MNRAS*, 363, L1
- Garcia-Rissmann, A., Vega, L. R., Asari, N. V., et al. 2005, *MNRAS*, 359, 765
- Gonçalves, A. C., Collin, S., Dumont, A.-M., & Chevallier, L. 2007, *A&A*, 465, 9
- Gorjian, V., Cleary, K., Werner, M. W., & Lawrence, C. R. 2007, *ApJ*, 655, L73
- Groves, B. A., Dopita, M. A., & Sutherland, R. S. 2004a, *ApJS*, 153, 9
- Groves, B. A., Dopita, M. A., & Sutherland, R. S. 2004b, *ApJS*, 153, 75 (G04)
- Groves, B. A., Heckman, T. M., & Kauffmann, G. 2006, *MNRAS*, 371, 1559
- Gültekin, K., Richstone, D. O., Gebhardt, K., et al. 2009, *ApJ*, 698, 198
- Heckman, T. M. 1980, *A&A*, 87, 152
- Ho, L. C., Filippenko, A. V., & Sargent, W. L. W. 1996, *ApJ*, 462, 183
- Ho, L. C., & Peng, C. Y. 2001, *ApJ*, 555, 650
- Ho, L. C. 2008, *ARA&A*, 46, 475
- Kauffmann, G., et al. 2003, *MNRAS*, 346, 1055
- Kaspi, S., Maoz, D., Netzer, H., Peterson, B. M., Vestergaard, M., & Jannuzi, B. T. 2005, *ApJ*, 629, 61
- Keel, W. C., & Windhorst, R. A. 1991, *ApJ*, 383, 135
- Kelly, B. C., & Bechtold, J. 2007, *ApJS*, 168, 1
- Kewley, L. J., Dopita, M. A., Sutherland, R. S., Heisler, C. A., & Trevena, J. 2001, *ApJ*, 556, 121
- Kewley, L. J., Groves, B., Kauffmann, G., & Heckman, T. 2006, *MNRAS*, 372, 961 (K06)
- Kraemer, S. B., Crenshaw, D. M., Hutchings, J. B., et al. 2000, *ApJ*, 531, 278
- Kraemer, S. B., Trippe, M. L., Crenshaw, D. M., et al. 2009, *ApJ*, 698, 106
- Krolik, J. H., McKee, C. F., & Tarter, C. B. 1981, *ApJ*, 249, 422
- Krolik, J. H., & Vrtilik, J. M. 1984, *ApJ*, 279, 521
- Krolik, J. H. 1999, *Active galactic nuclei : from the central black hole to the galactic environment* /Julian H. Krolik. Princeton, N. J. : Princeton University Press, c1999.,
- Laor, A., & Draine, B. T. 1993, *ApJ*, 402, 441
- Laor, A. 2003, *ApJ*, 590, 86
- Lauer, T. R., Ajhar, E. A., Byun, Y.-I., et al. 1995, *AJ*, 110, 2622
- Lewis, K. T., & Eracleous, M. 2006, *ApJ*, 642, 711
- Liu, G., Zakamska, N. L., Greene, J. E., Nesvadba, N. P. H., & Liu, X. 2013, *MNRAS*, 430, 2327
- Liu, G., Zakamska, N. L., Greene, J. E., Nesvadba, N. P. H., & Liu, X. 2013, arXiv:1305.6922
- Mathews, W. G., & Blumenthal, G. R. 1977, *ApJ*, 214, 10
- Mathews, W. G. 1982, *ApJ*, 252, 39
- Mathews, W. G. 1986, *ApJ*, 305, 187
- Marziani, P., Sulentic, J. W., Dultzin-Hacyan, D., Calvani, M., & Moles, M. 1996, *ApJS*, 104, 37
- Marziani, P., Sulentic, J. W., Zamanov, R., et al. 2003, *ApJS*, 145, 199
- Massaro, F., Chiaberge, M., Grandi, P., et al. 2009, *ApJ*, 692, L123
- Mathews, W. G., & Ferland, G. J. 1987, *ApJ*, 323, 456
- Mazzalay, X., Rodríguez-Ardila, A., & Komossa, S. 2010, *MNRAS*, 405, 1315
- Mazzalay, X., Rodríguez-Ardila, A., Komossa, S., & McGregor, P. J. 2013, *MNRAS*, 430, 2411
- Meléndez, M., Kraemer, S. B., Schmitt, H. R., et al. 2008, *ApJ*, 689, 95
- Molina, M., Bassani, L., Malizia, A., et al. 2009, *MNRAS*, 399, 1293
- Nagao, T., Murayama, T., Shioya, Y., & Taniguchi, Y. 2003, *AJ*, 125, 1729
- Narayan, R., & Yi, I. 1995, *ApJ*, 452, 710
- Nelson, C. H., & Whittle, M. 1995, *ApJS*, 99, 67
- Netzer, H., & Laor, A. 1993, *ApJ*, 404, L51
- Nussbaumer, H., & Osterbrock, D. E. 1970, *ApJ*, 161, 811
- Onken, C. A., Ferrarese, L., Merritt, D., et al. 2004, *ApJ*, 615, 645
- Pellegrini, E. W., Baldwin, J. A., Brogan, C. L., et al. 2007, *ApJ*, 658, 1119
- Pellegrini, E. W., Baldwin, J. A., & Ferland, G. J. 2011, *ApJ*, 738, 34
- Rees, M. J. 1987, *MNRAS*, 228, 47P
- Rees, M. J., Netzer, H., & Ferland, G. J. 1989, *ApJ*, 347, 640
- Richards, G. T., et al. 2006, *ApJS*, 166, 470
- Rózańska, A., Goosmann, R., Dumont, A.-M., & Czerny, B. 2006, *A&A*, 452, 1
- Schmitt, H. R., Donley, J. L., Antonucci, R. R. J., Hutchings, J. B., & Kinney, A. L. 2003, *ApJS*, 148, 327
- Scoville, N., & Norman, C. 1995, *ApJ*, 451, 510
- Shields, J. C., Pogge, R. W., & De Robertis, M. M. 1999, *Structure and Kinematics of Quasar Broad Line Regions*, 175, 353
- Shields, G. A., Ludwig, R. R., & Salvander, S. 2010, *ApJ*, 721, 1835
- Steffen, A. T., Strateva, I., Brandt, W. N., Alexander, D. M., Koekemoer, A. M., Lehmer, B. D., Schneider, D. P., & Vignali, C. 2006, *AJ*, 131, 2826
- Stern, J., & Laor, A. 2012a, *MNRAS*, 423, 600
- Stern, J., & Laor, A. 2012b, *MNRAS*, 426, 2703



Stern, J., & Laor, A. 2013, MNRAS, 431, 836  
 Sulentic, J. W., Bachev, R., Marziani, P., Negrete, C. A., & Dultzin, D. 2007, ApJ, 666, 757  
 Stoklasová, I., Ferruit, P., Emsellem, E., et al. 2009, A&A, 500, 1287  
 Suganuma, M., Yoshii, Y., Kobayashi, Y., et al. 2006, ApJ, 639, 46  
 Telfer, R. C., Zheng, W., Kriss, G. A., & Davidsen, A. F. 2002, ApJ, 565, 773  
 Tueller, J., Mushotzky, R. F., Barthelmy, S., et al. 2008, ApJ, 681, 113  
 Vanden Berk, D. E., Richards, G. T., Bauer, A., et al. 2001, AJ, 122, 549  
 Veilleux, S., & Osterbrock, D. E. 1987, ApJS, 63, 295  
 Veilleux, S., Rupke, D. S. N., Kim, D.-C., et al. 2009, ApJS, 182, 628  
 Vestergaard, M., & Peterson, B. M. 2006, ApJ, 641, 689  
 Villar-Martin, M., & Binette, L. 1997, A&A, 317, 350  
 Verdolini, S., Yeh, S. C. C., Krumholz, M. R., Matzner, C. D., & Tielens, A. G. G. M. 2013, ApJ, 769, 12  
 Walsh, J. L., Barth, A. J., Ho, L. C., et al. 2008, AJ, 136, 1677  
 Weaver, K. A., Meléndez, M., Mushotzky, R. F., et al. 2010, ApJ, 716, 1151  
 Weymann, R. 1976, ApJ, 208, 286  
 Whittle, M., & Saslaw, W. C. 1986, ApJ, 310, 104  
 Willett, K. W., Stocke, J. T., Darling, J., & Perlman, E. S. 2010, ApJ, 713, 1393  
 Yeh, S. C. C., Verdolini, S., Krumholz, M. R., Matzner, C. D., & Tielens, A. G. G. M. 2013, ApJ, 769, 11  
 Young, A. J., Wilson, A. S., & Shopbell, P. L. 2001, ApJ, 556, 6  
 Zakamska, N. L., Strauss, M. A., Krolik, J. H., et al. 2003, AJ, 126, 2125  
 Zhou, X.-L., & Wang, J.-M. 2005, ApJ, 618, L83

## APPENDIX A: IONIZATION STRUCTURE

Figure A1 shows the ionization structure vs.  $\tau$ , for the dusty RPC model shown in Fig. 2. Note the large range of ionization, which implies that X-ray line emission (e.g.  $O^{7+}$ ), ‘coronal’ line emission (e.g.  $Ne^{4+}$ ), and [O III] emission can come from the same slab. Because the ionization structure is set to first order by  $\tau$  (eq. 11), other reasonable choices of  $n_\gamma$ ,  $Z$  or  $\alpha_{ion}$  have only a secondary effect on the implied ionization structure.

## APPENDIX B: ESTIMATES OF $M_{BH}$ , $L_{ion}$ AND $\sigma_*$

The references for the  $\sigma_*$  and  $M_{BH}$  estimates used in Fig. 8 are listed in Table B1. In case of multiple measurements of the same quantity, we use the average value. In M 81 the estimate of  $M_{BH}$  is based on gas and stellar dynamics. In other objects, if a measurement of  $\sigma_*$  is available we use the Gültekin et al. (2009) relation to estimate  $M_{BH}$ . Otherwise, we use  $M_{BH}$  estimates based on the bulge luminosity (PKS 1718-649) or the virial assumption of the BLR (MR 2251-178 and PG 2251+113).

To estimate  $L_{ion}$  in all objects consistently, we use the measured flux of either the broad  $H\alpha$  or broad  $H\beta$ , which are available for seven of the eight objects in Fig. 8. The Balmer lines are preferred also because they are less sensitive to reddening and stellar contamination effects than UV continuum observations. We assume  $H\alpha/H\beta = 3$ , a FRW cosmology with  $\Omega = 0.3$ ,  $\Lambda = 0.7$

Object	Ref. for $\sigma_*$	Ref. for $M_{BH}$	Balmer line	$\frac{L_{ion}(\text{continuum})}{L_{ion}(\text{Balmer})}$
M 81	1	6,7	broad $H\alpha$	0.6
PKS 1718-649	<i>a</i>	8	narrow $H\alpha^b$	3 <sup>d</sup>
NGC 7213	2	<i>a</i>	broad $H\alpha$	1.4
Pictor A	3	<i>a</i>	broad $H\alpha^{b,c}$	0.5
NGC 3783	4, 5	<i>a</i>	broad $H\beta$	2.2
Ark 120	4	<i>a</i>	broad $H\beta$	0.8
MR 2251-178	<i>a</i>	9,10	broad $H\beta$	0.5
PG 2251+113	<i>a</i>	11,12	broad $H\beta$	1.1

**Table B1.**

Notes:

<sup>a</sup> The value of  $\sigma_*$  is based on  $M_{BH}$ , or vice-versa, using the Gültekin et al. (2009) relation.

<sup>b</sup> Measurements were taken in non-photometric conditions.

<sup>c</sup> We assume the broad  $H\alpha$  flux is 70% of the quoted total (broad+narrow)  $H\alpha$  flux.

<sup>d</sup> Continuum-based measurement is an upper limit.

References: 1. Gültekin et al. (2009); 2. Nelson & Whittle (1995); 3. Lewis & Eracleous (2006); 4. Onken et al. (2004); 5. Garcia-Rissmann et al. (2005); 6. Bower et al. (2000); 7. Devereux et al. (2003); 8. Willett et al. (2010); 9. Zhou & Wang (2005); 10. Kelly & Bechtold (2007); 11. Vestergaard & Peterson (2006); 12. Davis & Laor (2011).

and  $H_0 = 70 \text{ km s}^{-1} \text{ Mpc}^{-1}$ , and  $L_{ion}/L_{bH\alpha} = 45$ , appropriate for our assumed SED and the bolometric correction factor for  $L_{bH\alpha}$  found by Stern & Laor (2012a). For simplicity, we disregard possible changes in  $L_{ion}/L_{bH\alpha}$  with  $L_{bol}$ . If available, we use the Balmer line flux measurements from the same spectrum which was used to measure the  $\nu$  of the NLR (see references in Table 1). In NGC 3783 and Ark 120 the Balmer fluxes are not available in these spectra, so the broad  $H\beta$  flux is taken from Marziani et al. (2003). In PKS 1718-649, the broad Balmer lines are not detected. We therefore use the narrow  $H\alpha$  flux measured by Filippenko (1985), together with the Laor (2003) conversion between  $L_{nH\alpha}$  and  $L_{bol}$ . The Balmer line used in each object is listed in Table B1.

To verify our  $L_{ion}$  estimates, we estimate  $L_{ion}$  also from *HST* measurements of continuum luminosities. Sulentic et al. (2007) lists the *HST* continuum flux at 1550Å of Pictor A, NGC 3783, Ark 120, MR 2251-178 and PG 2251+113. For NGC 7213 and M 81 we use the V-band and B-band *HST* measurements from Lauer et al. (1995) and Ho & Peng (2001), respectively. In PKS 1718-649, only an upper limit on the continuum flux at 1200Å is available (from Keel & Windhorst 1991, using *IUE*). We use the bolometric correction factors from Richards et al. (2006), again disregarding possible changes in the SED with  $L_{bol}$ . The continuum-based  $L_{ion}$  estimates of the seven objects with detections are consistent with the Balmer-based  $L_{ion}$  estimates to within a factor of 2.2 (Table B1). A factor of two error in  $L_{ion}$  will change the expected  $\nu$  in the  $\nu$  vs.  $n_{crit}$  relation (eq. 28) by 20%, significantly less than the factor of  $3^{1/2}$  uncertainty in  $\nu$  due to the assumed uncertainty in  $M_{BH}$ .

## APPENDIX C: EMISSION LINE RATIOS

The observed emission line ratios which appear in Fig. 9 are assembled as follows. The observed optical [Ne V], [O III] and [O I] luminosities are taken from the Stern & Laor (2012a) sample of  $z < 0.3$  broad line AGN, which was selected from the 7<sup>th</sup> data release of the SDSS (Abazajian et al. 2009) based on the detection of broad  $H\alpha$  emission. The [O III] detection rate is 99.7%.



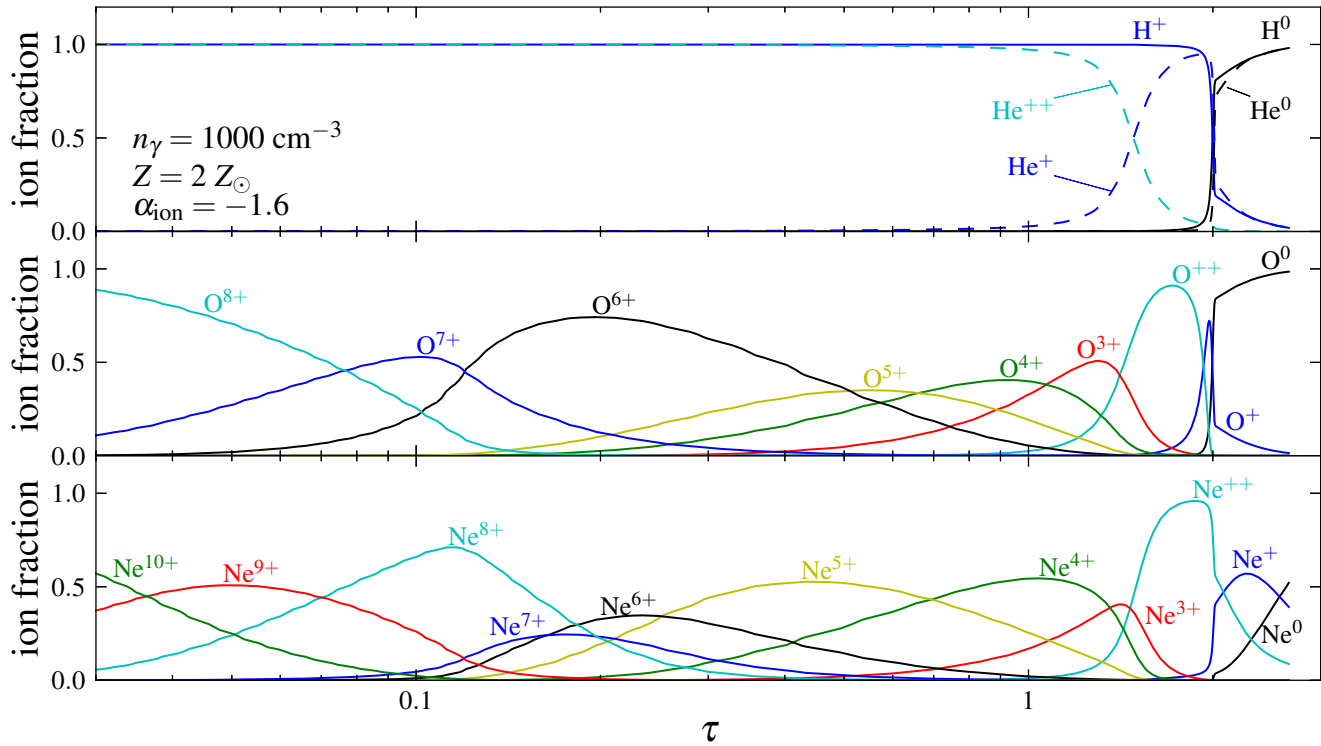


**Figure A1.** The H, He, O, and Ne ionization structure vs. optical depth, for the RPC model shown in Fig. 2. The broad range of ionization states implies that the same slab emits X-ray lines, ‘coronal’ lines and low ionization optical lines. Other reasonable choices of  $n_\gamma$ ,  $Z$  or  $\alpha_{\text{ion}}$  have only a secondary effect on the implied ionization structure.

In the  $z > 0.15$  objects where [Ne v] enters the SDSS spectrum, the [Ne v] detection rate is 96%. We use the Stern & Laor [O III] measurements, and the SDSS pipeline measurements of [Ne v]. We find  $\log[\text{Ne v}]/[\text{O III}] = -0.79 \pm 0.4$  (one-sigma range) in the 973  $z > 0.15$  objects, and  $\log[\text{Ne v}]/[\text{O III}] = -0.95 \pm 0.4$  in the 172 objects with  $L_{i,45} > 1$ . For comparison, Nagao et al. (2003) find similar  $\log[\text{Ne v}]/[\text{O III}] = 0.82 \pm 0.32$  on 34 local AGN, Zakamska et al. (2003) find a mean  $\log[\text{Ne v}]/[\text{O III}] = -0.92$  in type 2 quasars, and Vanden Berk et al. (2001) find a mean value of  $-0.8$  in SDSS quasars. The [O I] emission line is detected in 76% of the sample. We find  $\log[\text{O III}]/[\text{O I}] = 1.1 \pm 0.3$ , taking upper limits in objects with no detections. The mean  $[\text{O III}]/[\text{O I}]$  in the  $L_{i,45} > 1$  objects is 1.2, though the [O I] detection rate is 55%. Vanden Berk et al. (2001) and Zakamska et al. (2003) find a similar mean  $\log[\text{O III}]/[\text{O I}] = 1.1$  and 1.0, respectively.

The IR [Ne III], [Ne v], and [Ne VI] fluxes are taken from the 36 PGs in the QUEST (Veilleux et al. 2009) sample. We find  $\log[\text{Ne v}]/[\text{Ne III}] = -0.3 \pm 0.2$  in the 35 objects with a [Ne III] detection. In the eight objects without a [Ne v] detection, the  $3\sigma$  upper limits are used. Similar values of  $[\text{Ne v}]/[\text{Ne III}]$  were found by Gorjian et al. (2007), in AGN which span four orders of magnitude in [Ne v] luminosity. Also, Weaver et al. (2010) found a similar  $\log[\text{Ne v}]/[\text{Ne III}] \approx -0.4$  in 130 AGN with lower luminosities than the PGs, selected by their hard X-ray emission. In seven of the 35 PGs, [Ne VI] was observed, and detected in all objects. We find  $\log[\text{Ne VI}]/[\text{Ne III}] = -0.06 \pm 0.25$  in these objects.